The resting state of the human T-cell receptor

Ryan Q. Notti[1,2,*], Fei Yi[3,4], Søren Heissel[5], Henrik Molina[5], Christopher A. Klebanoff[2,3,4], and Thomas Walz[1]

[1] Laboratory of Molecular Electron Microscopy, The Rockefeller University, New York, NY

[2] Department of Medicine, Memorial Sloan Kettering Cancer Center, New York, NY

[3] Human Oncology Pathogenesis Program, Memorial Sloan Kettering Cancer Center, New York, NY

[4] Parker Institute for Cancer Immunotherapy, Memorial Sloan Kettering Cancer Center, New York, NY

[5] Proteomics Resource Center, The Rockefeller University, New York, NY

* To whom correspondence should be addressed: rnotti@rockefeller.edu

Summary

The T-cell receptor (TCR) is central to the ligand-dependent activation of T lymphocytes and as such orchestrates both adaptive and pathologic immune processes[1]. However, major questions remain regarding the structure and function of the human TCR[2–4]. Here, we present cryogenic electron microscopy structures for the unliganded human TCR in a native-like lipid bilayer, revealing three related conformations that are distinct from previously reported structures of receptors in detergent. These new "closed and compacted" conformations afford insights into the interactions between the TCR and the membrane, including conserved surface patches that make extensive outer leaflet contact, and suggest novel conformational regulation by glycans. We show that the closed/compacted conformations, not the extended one previously reported in detergent[5–8], represent the unliganded resting state for the TCR *in vivo*, underscoring the importance of structural interrogation of membrane proteins in native-like environments. We use

conformation-locking disulfide mutants to show that juxtamembrane linker extension is necessary for ligand-dependent TCR activation, demonstrating that TCR-intrinsic conformational change is necessary for TCR activation and opening numerous avenues for immunoreceptor engineering.

Main

T cells are central to a wide array of both adaptive and pathologic immune responses. The T-cell receptor (TCR) allows T cells to recognize and respond to antigenic peptides presented on human leukocyte antigen (HLA) complexes of other cells. While the identities of the TCR constituents and its downstream signaling elements have been known for some time, questions remain regarding its activation mechanism.

The TCR is a hetero-octameric membrane protein complex[5–8]. The αβ-type TCR is comprised in part by two variable chains, TCRα and TCRβ, which directly interface with the peptide-HLA complex. Antigen specificity is generated through somatic recombination of the variable segments in the TCRα and TCRβ genes. The remainder of the core complex is comprised of six invariant CD3 family chains: a CD3γ-CD3ε heterodimer, a CD3δ-CD3ε heterodimer, and a CD3ζ homodimer. Herein, we differentiate the CD3ε protomers by the CD3 component with which each pairs ($CD3\varepsilon_D$ pairs with CD3δ, and $CD3\varepsilon_G$ pairs with CD3γ) and the CD3ζ protomers as CD3ζ and CD3ζ'.

While the TCRα and TCRβ chains lack intracellular signaling domains, the CD3 proteins possess cytoplasmic immunoreceptor tyrosine activation motifs (ITAMs) that become phosphorylated upon TCR-HLA interaction and then bind and activate downstream signaling kinases. Dynamic interactions between ITAMs and the membrane regulate signaling[9,10], but the mechanism by which ligand binding to the extracellular TCRα-TCRβ domains results in

phosphorylation of cytoplasmic CD3 ITAMs remains a matter of debate. Specifically, it is unclear whether ligand binding and activation involves conformational change in the TCR complex. While reconstitution of TCR signaling *in vivo* with minimal constructs has argued against transmembrane conformational change[11], evidence for reversible structural extension of the TCR under mechanical force suggests the opposite[12], although the structural details remain to be determined.

Structures of the hetero-octameric αβ-type TCR (herein, TCR) have been determined by cryogenic electron microscopy (cryo-EM)[5–8]. These studies revealed an antenna-like structure, with the TCRα and TCRβ variable domains projecting over a ring formed by the CD3 ectodomains and the TCRα and TCRβ constant domains, with numerous interactions between their respective transmembrane (TM) helices (Extended Data Figure 1a). Addition of peptide-HLA to this complex did not meaningfully alter the conformation of the TCR[7,8], arguing against models of intrinsic conformational change in the ligand-dependent TCR activation process (Extended Data Figure 1a,b).

However, the TCR complexes used in these studies were solubilized in detergent. Biochemical data have previously shown important roles for the lipid bilayer in the regulation of TCR signaling specifically[6,14,15], raising questions as to the physiologic relevance of the determined structures. Membrane protein structure determination is generally preferable in a native-like membrane environment that increases the likelihood that important protein–lipid interactions are captured in the obtained molecular models[16].

Here, we report near-atomic resolution structures of human TCR obtained in a native-like lipid environment. The structures reveal novel conformations, distinct from those previously reported, and cross-linking data support the notion that these conformations represent the resting state of an unstimulated TCR on T cells. We hypothesize that the previously published

structures of the TCR in detergent approximate a ligand-activated conformation and show that exit from the resting state conformation is required for TCR signaling.

Results

Structure of the TCR in a native-like lipid environment. We reconstituted the TCR complex into proteolipid nanodiscs loaded with mammalian polar lipids and cholesteryl hemisuccinate to form a native-like bilayer environment (Extended Data Figure 1c-f, Supplementary Methods). We used a derivative of the 1G4 TCR specific to the NY-ESO-1 cancer-testis antigen, as it is both a model immunoreceptor and being developed as an anti-cancer therapeutic[17]. Computational processing of cryo-EM data yielded three maps determined to nominal resolutions of 3.2 to 3.5 Å (Extended Data Table 1, Extended Data Figures 2-4, Supplementary Methods). These maps were clearly different from the previously published TCR structures and attempts to bias the particle search towards the published conformations with projections of the structure in detergent or that same structure docked into a lipid nanodisc model did not yield any maps approximating the previously published conformation (Extended Data Figure 2).

Molecular models were built for the three highest resolution 3D maps by docking previously determined cryo-EM and crystallographic structures into the maps and refining them by standard approaches (Extended Data Table 1, Extended Data Figure 5, Supplementary Methods). These models revealed three distinct but related conformations of the TCR, herein nanodisc (ND) 1, ND2, and ND3 (Figure 1a, Extended Data Figure 6a), named in series from least similar (ND1) to most similar (ND3) to the conformation of the TCR in detergent. For the highest resolution structure (ND3), all ectodomains, JM linkers, and TM helices were modeled, except for the carboxy termini of the TM helices near the membrane/solvent interface, which showed poor density, and portions of the TCRα and TCRβ JM linkers (see below).

The ND conformations show two large conformational changes relative to that in detergent: a “closure” of the TCR ectodomains against the CD3 ectodomains (Figure 1a,b) and a “compaction” of the juxtamembrane (JM) linker peptides (Figure 1a,c,d). Collectively, these changes shorten the TCR projection into the extracellular milieu by approximately 35 Å (Figure 1a, Extended Data Figure 6a,b). Closure of the TCR ectodomains results in part from an 18-22° rotation of the variable domains towards their respective constant domains about the interdomain hinge region (Extended Data Figure 6c). Relative to the “extended” JM linker conformations seen in detergent, the CD3 JM linkers are compacted, with closer approximation of the CD3 ectodomains to the amino-terminal ends of their TM helices, distorting their helical character (Figure 1c). In contrast to the TCRα and TCRβ JM linkers in detergent, which are structured throughout their course, these regions in ND1-3 were only visible from the TCR constant domains out to their interchain disulfide linkage (Extended Data Figure 6e).

The conformational changes in the TCR ectodomains are accompanied by rotations of TM helices. While the in-plane arrangement of the TM helices is largely similar when viewed along the membrane normal (Figure 1e), examination from orthogonal axes reveals differences in TM helix conformation. Compaction of the CD3 JM linkers requires opening of the angle between the TM helices of the CD3εδ and CD3εγ pairs by 21° (from 32º to 53º) and 17° (from 37º to 54º), respectively (Figure 1d and Extended Data Figure 6d). Additionally, there is similar splaying of the TCRβ and distal CD3ζ TM helices away from the membrane normal (Figure 1e,g). In detergent, the TCRα and TCRβ TM helices extend outward past the amino-terminal ends of the CD3 TM helices, where they are ensconced by the extended CD3 JM linkers (Figure 1f). Compaction of the JM linkers in ND1-3 necessitates reorganization of these TCRα and TCRβ TM regions, which are unstructured and displaced towards the lipid bilayer (Figure 1g). We note that the unstructured TCR JM linkers preclude continuous modeling of the TCRα and

TCRβ sequences from the ectodomains through to the TM helices, and without atomic resolution in this region we cannot assign the register of the TCR TM sequences with complete certainty. We assigned the initial sequence register by docking of the micelle-to-nanodisc-aligned TCR model (Extended Data Figure 6b). We believe this to be the most conservative, parsimonious, and biologically plausible model for the TCR TM helices in the lipid bilayer, as it retains the insertion position of the TM helices within the hydrophobic bilayer/micelle environment (Extended Data Figure 6b,f) as well as the key contacts between the TCR and CD3 TM helices shown in the previously published structures. Taken together, these cryo-EM maps reveal marked conformational differences between the TCR in a lipid bilayer and those previously reported in detergent micelles.

Lipid interactions with the TCR. The TCR is known to interface directly with membrane cholesterol, and the binding sites have been visualized in previously published structures[6]. In the nanodisc native-like membrane environment, density corresponding to two cholesterols was again apparent (Extended Data Figure 7a). The two cholesterol molecules are oriented tail-to-tail in a groove between CD3ζ', TCRα, TCRβ, and CD3γ, as in detergent micelles (Figure 2a). However, the compaction-associated changes in the TCR TM helices result in a sliding of the cholesterol molecules towards each other, with deflection of their branched aliphatic tails to prevent clashing (Figure 2a, insets). We refer to the cholesterol molecules as $Chol_A$ and $Chol_B$, corresponding to the TCR TM helix with which each is approximated (Extended Data Figure 7b). The deflected tails are interposed between adjacent TM helices, accommodated by their increased splay in the compact conformation (Figure 2b, right). The cholesterol-binding groove is more open to the membrane bilayer in nanodiscs, creating a possible path for cholesterol

loading into the assembled TCR and/or exchange with the membrane environment (asterisks in Figure 2b).

Imaging of the TCR in a lipid bilayer revealed additional sites of protein–lipid interaction. Unmodeled tubular densities consistent with phospholipid acyl chains are present at several sites adjacent to the TCR TM helices (yellow densities, Figure 2c,e and Extended Data Figure 9c,d). Structured lipid is seen parallel to the tail-to-tail cholesterol dimer, filling the aforementioned channel between the cholesterol-binding groove and the membrane bilayer (Figure 2c). Splay of the CD3ζ TM helix away from that of CD3ε_D enlarges and extends a cavity seen in the TCR in detergent (Figure 2d), which is filled by three lipid acyl chains in the nanodisc (Figure 2e). This cleft is narrowed and displaced towards the carboxy termini of the CD3ζ and CD3ε_D TM helices in the detergent structure, but three tubular densities are seen in the previously published maps as well, which may represent endogenous lipid acyl chains or molecules of *n*-dodecyl-β-D-maltopyranoside detergent (Figure 2e). Additional probable sites of structured lipid include a shroud of density over the CD3ζ TM helices (Extended Data Figure 7c) and in the cleft over the TCRαβ TM helices between CD3δ and CD3ε_G (Extended Data Figure 7d). Cys124 is a site of known palmitoylation at the carboxy terminus of the CD3δ TM helix[18], and density corresponding to the palmitic acid chain was seen in the previously published structures (Extended Data Figure 7e). Cys124 is not visible in our structures, precluding definitive assignment of the palmitate density; however, analogous density is seen in our maps (Extended Data Figure 7d, asterisk).

The ND1-3 maps show clear density for the proteolipid nanodisc that enshrouds not only the TM helices, but also the membrane proximal faces of the TCR ectodomains (Figure 3a, left). The lipid contacts with the CD3 ectodomains are apparent even in maps contoured at a higher threshold, consistent with high occupancy (Figure 3a, right). While the CD3 ectodomain

surfaces are generally poorly evolutionarily conserved in comparison to the TM helices, patches on the membrane-proximal surfaces of the CD3 ectodomains do show high sequence conservation (Figure 3a,b). These highly conserved ectodomain surface patches (black triangles in Figure 3b-e) interface with the extracellular membrane leaflet and are neutral to electropositive (Figure 3d,e), facilitating phospholipid head group interactions. Of note, we observe a similar conserved electropositive patch at the interface of CD79αβ[19], the analogous ITAM-bearing chains in the B-cell receptor, raising the prospect that this interface may also favor membrane interactions and a different conformation in the lipid bilayer from that reported in detergent micelles (Extended Data Figure 7f-i).

Probing TCR conformation in situ. Which conformation of the TCR is the physiologic resting state on the cell membrane: the open/extended conformation seen in detergent micelles, or the closed/compacted conformations seen in the lipid bilayer of the nanodisc? Given that the lipid bilayer of a nanodisc more closely approximates the physicochemical milieu of the plasma membrane, we hypothesized that the TCR is closed and compacted in the absence of activating ligand *in vivo.* To test this notion, we engineered a series of disulfide bonds that would only be geometrically favorable in one conformation or the other and read out their presence or absence by one of the following approaches: (1) non-reducing sodium dodecyl sulfate-polyacrylamide gel electrophoresis (SDS-PAGE) and Western blot of whole cell lysates for interchain disulfides, or (2) mass spectrometry on affinity-purified protein for intrachain disulfides. Analysis of disulfide bonds in the Protein Databank have shown that disulfide bonds almost never have a Cys-Cys Cα-Cα distance greater than 7 Å, with most being between 5 and 6.5 Å[20]. Accordingly, we sought residue pairs in the TCR ectodomains with Cα-Cα distances below 7 Å in one conformation and above 7 Å in the other as candidates for disulfide engineering.

The interface between CD3δ and TCRα contained several pairs of residues with geometry favorable for engineered disulfide formation in ND1 but not between the homologous residues in the structures in detergent (Figure 4a). As TCRα and TCRβ are linked by an interchain disulfide natively, formation of a TCRα–CD3δ disulfide would result in an upward gel shift of the TCRαβ heterodimer in nonreducing SDS-PAGE. For all three tested engineered disulfide pairs meeting these geometric constraints, a gel shift consistent with TCRα–CD3δ disulfide formation was observed (Figure 4b). Confirming that this mass shift was due to disulfide formation, no gel shift was apparent under reducing conditions (Extended Data Figure 8a). Moreover, the mass shift was due to the formation of the engineered disulfide and not an off-target bond, as adduct formation was only seen when both residues in a given target pair were mutated to cysteines (Figure 4b). As an internal negative control, a permutation of cysteine mutants at this interface not meeting geometric criteria for disulfide formation in ND1 (TCRα S78C – CD3δ N38C, Figure 4a, right, orange labels) was produced. It did not form a disulfide *in vivo* (Figure 4b, orange) despite S78C and N38C successfully pairing with cognate cysteine mutants that did meet the inter-Cα threshold. This control shows the structural precision and specificity of the engineered disulfide bond approach.

The region around the TCRα and TCRβ interdomain hinges is also notably different in the closed/compacted conformation compared to the open/extended one, with the variable domains coming into closer apposition with their respective constant domains (Extended Data Figure 6c), allowing the engineering of conformation-specific disulfide pairs in this region (Figure 4c,d). We probed formation of these intrachain disulfides by mass spectrometry. Proteolytic digestion of the TCR with trypsin and chymotrypsin yielded distinct peptides, several of which were linked by disulfide-bonds. Electron-transfer/higher-energy collision dissociation (EThcD) fragmentation was used to fragment the disulfide-bonded peptides providing *in vacuo* reduction

to the linear peptide constituents along with peptide backbone fragmentation, thereby allowing unambiguous identification of the engineered disulfides[21]. All native TCR disulfides spanning two proteolytic fragments (Extended Data Figure 8b) were observed in the wild-type 1G4 TCR by this approach (Extended Data Table 2). For both ND conformation-compatible engineered disulfides tested (Figure 4c,d), we observed formation of the engineered disulfide (Figure 4e,f and Extended Data Table 2). In contrast, an engineered disulfide that would only be present in the open/extended conformation (Extended Data Figure 8c) did not form *in vivo* (Extended Data Table 2). Taken together, these data support the conclusion that a TCR in the unliganded, resting state adopts the closed/compact conformation *in vivo*.

Conformational variability of the TCR in a lipid bilayer. We observed three conformations for the closed/compacted TCR, denoted ND1-3. Comparison of the three structures reveals a stepwise series of motions that would allow exchange between these conformations (Figure 5a, Supplementary Movie 1). ND1 is the most closed of the three structures, and transition to ND2 requires the depression of the CD3ε_D ectodomain away from the TCR variable domains and towards the bilayer outer leaflet (Figure 5a). Transition from ND2 to ND3 requires opening of the TCR interdomain hinge and elevation of the TCR constant domains. These ectodomain movements are accompanied by shifting or rearward rotation of the TCRα, TCRβ, CD3ε_D, and CD3γ TM helices, encroaching on the cholesterol-binding domain (Figure 5b, Extended Data Figure 9a,b). To accommodate this movement, there is rotation of Chol$_A$ and elevation of both cholesterols (Figure 5c), showing cholesterol to be an integral and dynamic component of the TCR structure.

The ND1-3 maps show an array of densities lateral to the CD3δ and TCRα ectodomains, corresponding to sites of known asparagine-linked glycosylation. Comparison of this region in

ND1-3 shows clear reorganization of the glycans (Figure 5d), with increased stacking of adjacent glycans brought into close proximity by tight ectodomain closure in ND1. In ND2 and ND3, the TCRα N82-linked and CD3δ N74-linked glycans are visible, emerging radially from the TCR, whereas the CD3δ N38-linked glycan is oriented inward towards the inside of the cleft between the TCR and CD3 ectodomains (Figure 5e, left and middle). This is the orientation of the CD3δ and TCRα glycans observed in the open/extended conformation (Extended Data Figure 9c). By contrast, in the tightly closed ND1 conformation, the CD3δ N38-linked glycan is extruded from the closed cleft and is oriented away from the ectodomains (Figure 5e, right), contributing to the stack of glycan density observed adjacent to that ectodomain surface. The CD3δ N74-linked glycan also visibly protrudes into the stack of glycan density. While TCRα N82 is also adjacent to the glycan stack, core asparagine-linked glycan density was not visible projecting from this residue, so it is unclear whether the TCRα N82-linked glycan contributes to the array of density.

The differences in ectodomain closure seen between ND1, ND2, and ND3 have consequences for the accessibility of the TCR variable domains to HLA-antigen complexes. In isolation, the TCR variable domains themselves show little change in structure in our models. Despite the graded movements of the TCR variable domains about the interdomain hinge, there is little change in the orientations of the TCR variable domains relative to one another throughout the ND series or when compared to the 1G4-HLA crystal structure[22] (Extended Data Figure 9d,e). To assess the impact of the CD3 ectodomains on TCR–HLA interactions, we modeled the binding geometry of HLA onto ND1-3 by alignment of the 1G4-HLA-antigen crystal structures with the variable domains of ND1-3. While the TCR variable domains in ND2 and ND3 appear well positioned to interact with HLA, clashing between HLA and the elevated CD3ε_D ectodomain in ND1 would preclude optimal HLA binding (Figure 5f).

A model for TCR conformational change in TCR activation. Taking the above structural, biochemical, and modeling data together and in context with the literature, we developed a model for ligand-dependent activation of the TCR. Our data support a model in which the unliganded TCR explores a series of thermally accessible closed/compacted conformations from the most closed and HLA-binding incompetent ND1 to the more open and HLA "receptive" ND3. Previous data have shown HLA monomer binding to the TCR is insufficient to drive T-cell activation, but that subsequent force application induced activation[23]. This activation was accompanied by an increase in TCR length normal to the membrane[12], raising the possibility that the open/extended structure of the TCR reported in detergent micelles is actually an approximation of a physiologically active state. Thus, we hypothesize that HLA-antigen binding and force application results in a structural transition from the receptive but closed/compact conformation (ND3) to an active extended conformation (Det, Figure 6a). Morphing the structure of ND3 to Det (Supplementary Movie 2, Figure 6a inset) shows straightening of the TM helices towards the membrane normal (that is, decreased splay) and elevation of the CD3εδγ TM helices relative to those of TCRα and TCRβ. These changes in TM conformation add to the plausibility of the model, as they provide a means to transmit conformational changes in the ectodomains to the cytoplasmic ITAMs.

Transition from the closed/compacted to the open/extended conformation would seem to require further ectodomain opening and JM linker extension (Figure 6a). To test the necessity of each of these two movements for ligand-dependent TCR activation, we again turned to engineered disulfide cross-linking. The introduction of the previously engineered intra-TCRα disulfide S104C–V182C (Figure 4c, 6c) would prevent ectodomain opening and a newly designed intra-TCRβ disulfide (Q220C–V274C, Figure 6b) would prevent extension (Figure 6c).

We introduced wild-type and mutant TCR constructs into TCRαβ-negative SUP-T1 T cells[24] using lentiviral transduction and assayed early T-cell activation by phospho-CD3ζ Western blotting. Surface localization and HLA-binding competence were confirmed by flow cytometry for the wild-type and both mutants (Extended Data Figure 10a). In the absence of HLA-antigen tetramers, there was no detectable CD3ζ phosphorylation in these cells (Figure 6d). Upon exposure to HLA-antigen tetramers, cells expressing either wild-type and the locked closed TCRα S104C–V182C mutant TCRs were activated, showing CD3ζ phosphorylation (Figure 6d). In contrast, the locked compacted TCRβ Q220C–V274C mutant did not demonstrate ligand-induced activation (Figure 6d, Extended Data Figure 10b,c). Importantly, both mutants showed CD3ζ phosphorylation upon non-specific phosphatase inhibition with pervanadate, indicating that the TCRβ Q220C–V274C mutant was properly assembled with CD3 on the cell surface, as the TCRαβ-negative SUP-T1 parental line lacks surface CD3 and shows no CD3ζ phosphorylation in response to pervanadate (Figure 6d).

Discussion

Here, we report structures of the human TCR in a lipid bilayer. We find that the TCR hetero-octamer assumes a series of more closed and compacted conformations relative to that previously reported in detergent micelles, that the closed/compacted conformation is indeed the native unliganded state of the TCR, and that exit from this conformation by JM linker extension is necessary for physiologic ligand-dependent activation of the TCR. While this latter finding does not rule out roles for TCR-extrinsic phenomena (e.g., higher-order clustering, steric exclusion of inhibitory phosphatases) in the activation of the TCR or regulation thereof, it argues that intrinsic conformational change in the TCR is necessary for early TCR activation and argues against previous models that have excluded this requirement.

Broadly, these findings reinforce the importance of structural interrogation of membrane proteins in lipid environments that closely resemble their physiologic environment. Comparison of TCRs in detergent micelles in the absence and presence of activating ligand had revealed no change in TCR structure, consistent with models excluding TCR conformational change in the activation process. Although these studies were technically well performed, our results now reveal that they did not identify the true resting state of the TCR, calling into question the conclusion that there is no intrinsic conformational change in the TCR during ligand-dependent activation.

Additionally, the structures in detergent did not capture the full scope of TCR interaction with the membrane. Not only are membrane lipids closely interwoven with the TM helices, but large conserved surface patches on the ectodomains mediate lipid–protein interactions, likely partially counteracting the thermodynamic costs of JM linker compaction and “spring loading” the TCR with potential energy for conformational change during activation. In this model, ligand binding and/or force application provides the activation energy to release the membrane-binding surfaces of the CD3 ectodomains and allow JM extension. This would be consistent with existing models of TCR response to force, which invoke conformational changes with free energy barriers rendering them inaccessible to thermal motion alone[13]. Detergent extraction would overcome this thermodynamic barrier by removing the lipid bilayer all together. During reconstitution into nanodiscs, we first extracted the TCR complex in detergent and presumably opened and extended the TCR, which suggests that the addition of a lipid bilayer is sufficient to reset the TCR to its resting conformation without the need for extrinsic chaperones. Lastly, we note that a similar conserved surface patch is present on the CD79 heterodimer in the B-cell receptor, raising the possibility that other hetero-multimeric ITAM-containing immunoreceptors exploit protein surface interactions with the lipid bilayer to constrain conformation.

As with the TCR structures in detergent, the CD3 ITAMs are not visible in our structures. The ITAMs are membrane-associated in the unliganded state[10,11], but are likely to be radially disordered along the intracellular membrane face. However, the TM helix movements seen between our closed/compacted and the open/extended conformations suggest a means for communication of extracellular conformational changes in the TCR complex to the ITAMs. Within the cytoplasmic domains of CD3 proteins, the basic residues proximal to the CD3 TM helix are critical for ITAM association with the membrane[10,11]. Upon transition from the receptive to the hypothesized active conformation, the decreased splay in the CD3 TM helices and their elevation relative to the TCR TM helices could alter basic patch interaction with the membrane and favor ITAM release.

Analysis of the basal conformational heterogeneity of the TCR suggests novel means of TCR regulation. The glycan stacking observed in the ligand-unreceptive resting conformation (ND1) is notably different from the glycan arrangement reported previously in the detergent environment and seen here in the more open ND2 and ND3 conformations. While molecular modeling of the branched glycan sugars was not possible with sufficient confidence, the stacked arrangement of glycan densities raises the possibility of extensive hydrogen bonding between the stacked glycans and perhaps also with TCR-surface residues. While glycan–glycan and glycan–protein interactions are well described *in trans*, there are fewer examples of structured glycan–glycan interactions within a given protein or stable complex – the human immunodeficiency virus-1 gp120 trimer is an example of the latter[25,26]. The stacking of glycans observed in the TCR is unique in being protein conformation-dependent. Breaking an extensive glycan hydrogen-bonding network to transition out of ND1 would be energetically costly, and thus modification of TCR glycosylation could serve as a means of posttranslational regulation of TCR activation threshold by increasing or decreasing the free energy barrier to ND1 exit.

Previous studies have explored the role of cholesterol in the regulation of TCR activation[6,15]. The substantive movements of the two cholesterol molecules seen between our resting and receptive conformations raise the possibility that changes in the sterol composition of the T-cell membrane (either global or local) could alter TCR activity even prior to ligand binding by shaping the basal TCR conformational landscape. Moreover, our structures reveal channels for cholesterol loading or exchange with the lipid bilayer not previously observed, making it plausible that already assembled TCR could respond to changes in membrane sterol content. Non-sterol lipid species are also known regulators of T-cell signaling[14], including phosphoinositol lipids[27,28] and oxidized lipids in the tumor microenvironment[29]. This work delineates multiple sites of structured interaction between the TCR and membrane lipids beyond the sterol-binding site, which may allow specific lipids to modulate TCR conformation and activity.

The extensive contacts between TCR variable-domain residues and those of the TCR constant domains or CD3 ectodomains in the closed/compacted conformations raises questions about how variation at these sites might confer specific baseline sensitivities to given TCR alleles. Whether use of certain V or J alleles changes the occupancy of different segments of the TCR conformational landscape will need to be determined and has broad implications for vaccine design and immunotherapy engineering. Likewise, whether individually rare germline coding variants in the TCR constant domain loci or CD3 proteins can affect an individual's basal T-cell reactivity is unclear outside of known deleterious loss-of-function alleles[30]. Such information might predict individual propensity for autoimmunity or responsiveness to immune-oncology agents and will provide insights for engineering TCRs with favorable activity profiles.

Methods

Full methods are detailed in the Supplementary Methods.

Data Availability Statement

Cryo-EM maps and atomic coordinates for ND1, ND2, and ND3 have been deposited in the Protein Data Bank and Electron Microscopy Data Bank with the following accession numbers: for ND1, PDB 8TW4, EMD-41658; for ND2, PDB 8TW5, EMD-41659; for ND3, PDB 8TW6, EMD-41660.

Acknowledgements

The authors thank the members of the Walz, T. de Lange (RU), and R. K. Hite (MSKCC) labs and Drs. E. L. Reinherz (HMS, DFCI) and W. D. Tap (MSKCC) for insightful conversations. We thank M. Ebrahim, J. Sotiris, and H. Ng at the Evelyn Gruss Lipper Cryo-EM Resource Center of The Rockefeller University for assistance with cryo-EM data collection. R.Q.N. was supported by National Institutes of Health (NIH) grants T32CA9207, KL2TR001865, and UL1TR001866; the Black Family Metastasis Center at Rockefeller University; the Shapiro-Silverberg Fund for the Advancement of Translational Research; and the Mark Foundation for Cancer Research (R.Q.N. and T.W.). C.A.K. was supported, in part, by NIH grants R37 CA259177, R01 CA269733, R01 CA286507, P30 CA008748, and P50 CA217694; the Parker Institute for Cancer Immunotherapy (F.Y. and C.A.K.); and The Sarcoma Center at MSKCC (C.A.K.). Mass spectrometry data was generated by the Proteomics Resource Center at The Rockefeller University (RRID:SCR_017797) using instrumentation funded by the Sohn Conferences Foundation and the Leona M. and Harry B. Helmsley Charitable Trust.

Author Contributions

R.Q.N conceived of the project, designed and performed experiments, analyzed data, built models, and wrote and revised the manuscript; F.Y. designed and performed experiments and

analyzed data; S.H. designed and performed experiments and analyzed data; H.M. designed and performed experiments and analyzed data; C.A.K. designed experiments, analyzed data, and revised the manuscript; T.W. designed experiments, analyzed data, and revised the manuscript.

Competing Interests

C.A.K. is an inventor on patents related to TCR discovery and public neoantigen-specific TCRs and is recipient of licensing revenue shared according to MSKCC institutional policies. C.A.K. has consulted for or is on the scientific advisory boards for Achilles Therapeutics, Affini-T Therapeutics, Aleta BioTherapeutics, Bellicum Pharmaceuticals, Bristol Myers Squibb, Catamaran Bio, Cell Design Labs, Decheng Capital, G1 Therapeutics, Klus Pharma, Obsidian Therapeutics, PACT Pharma, Roche/Genentech and T-knife. C.A.K. is a scientific co-founder and equity holder in Affini-T Therapeutics.

References

1. Janeway, C. A. *et al. Immunobiology*. (Garland Science, 2001).
2. Reinherz, E. L. The structure of a T-cell mechanosensor. *Nature* **573**, 502–504 (2019).
3. Courtney, A. H., Lo, W.-L. & Weiss, A. TCR Signaling: Mechanisms of Initiation and Propagation. *Trends Biochem. Sci.* **43**, 108–123 (2018).
4. Mariuzza, R. A., Agnihotri, P. & Orban, J. The structural basis of T-cell receptor (TCR) activation: An enduring enigma. *J. Biol. Chem.* **295**, 914–925 (2020).
5. Dong, D. *et al.* Structural basis of assembly of the human T cell receptor–CD3 complex. *Nature* **573**, 546–552 (2019).
6. Chen, Y. *et al.* Cholesterol inhibits TCR signaling by directly restricting TCR-CD3 core tunnel motility. *Mol. Cell* **82**, 1278-1287.e5 (2022).

7. Sušac, L. *et al.* Structure of a fully assembled tumor-specific T cell receptor ligated by pMHC. *Cell* **185**, 3201-3213.e19 (2022).
8. Saotome, K. *et al.* Structural analysis of cancer-relevant TCR-CD3 and peptide-MHC complexes by cryoEM. *Nat. Commun.* **14**, 2401 (2023).
9. James, J. R. & Vale, R. D. Biophysical Mechanism of T Cell Receptor Triggering in a Reconstituted System. *Nature* **487**, 64–69 (2012).
10. Xu, C. *et al.* Regulation of T Cell Receptor Activation by Dynamic Membrane Binding of the CD3ε Cytoplasmic Tyrosine-Based Motif. *Cell* **135**, 702–713 (2008).
11. Zhang, H., Cordoba, S.-P., Dushek, O. & Anton van der Merwe, P. Basic residues in the T-cell receptor ζ cytoplasmic domain mediate membrane association and modulate signaling. *Proc. Natl. Acad. Sci.* **108**, 19323–19328 (2011).
12. Das, D. K. *et al.* Force-dependent transition in the T-cell receptor β-subunit allosterically regulates peptide discrimination and pMHC bond lifetime. *Proc. Natl. Acad. Sci.* **112**, 1517–1522 (2015).
13. Reinherz, E. L., Hwang, W. & Lang, M. J. Harnessing αβ T cell receptor mechanobiology to achieve the promise of immuno-oncology. *Proc. Natl. Acad. Sci.* **120**, e2215694120 (2023).
14. Wu, W., Shi, X. & Xu, C. Regulation of T cell signalling by membrane lipids. *Nat. Rev. Immunol.* **16**, 690–701 (2016).
15. Wang, F., Beck-García, K., Zorzin, C., Schamel, W. W. A. & Davis, M. M. Inhibition of T cell receptor signaling by cholesterol sulfate, a naturally occurring derivative of membrane cholesterol. *Nat. Immunol.* **17**, 844–850 (2016).
16. Notti, R. Q. & Walz, T. Native-like environments afford novel mechanistic insights into membrane proteins. *Trends Biochem. Sci.* (2022).

17. Robbins, P. F. *et al.* A Pilot Trial Using Lymphocytes Genetically Engineered with an NY-ESO-1–Reactive T-cell Receptor: Long-term Follow-up and Correlates with Response. *Clin. Cancer Res.* **21**, 1019–1027 (2015).

18. Martin, B. R. & Cravatt, B. F. Large-Scale Profiling of Protein Palmitoylation in Mammalian Cells. *Nat. Methods* **6**, 135–138 (2009).

19. Su, Q. *et al.* Cryo-EM structure of the human IgM B cell receptor. *Science* **377**, 875–880 (2022).

20. Gao, X., Dong, X., Li, X., Liu, Z. & Liu, H. Prediction of disulfide bond engineering sites using a machine learning method. *Sci. Rep.* **10**, 10330 (2020).

21. Liu, F., van Breukelen, B. & Heck, A. J. R. Facilitating Protein Disulfide Mapping by a Combination of Pepsin Digestion, Electron Transfer Higher Energy Dissociation (EThcD), and a Dedicated Search Algorithm SlinkS*. *Mol. Cell. Proteomics* **13**, 2776–2786 (2014).

22. Chen, J.-L. *et al.* Structural and kinetic basis for heightened immunogenicity of T cell vaccines. *J. Exp. Med.* **201**, 1243–1255 (2005).

23. Kim, S. T. *et al.* The αβ T Cell Receptor Is an Anisotropic Mechanosensor *. *J. Biol. Chem.* **284**, 31028–31037 (2009).

24. Morgan, R. A. *et al.* High Efficiency TCR Gene Transfer into Primary Human Lymphocytes Affords Avid Recognition of Melanoma Tumor Antigen Glycoprotein 100 and Does Not Alter the Recognition of Autologous Melanoma Antigens. *J. Immunol.* **171**, 3287–3295 (2003).

25. Stewart-Jones, G. B. E. *et al.* Trimeric HIV-1-Env Structures Define Glycan Shields from Clades A, B, and G. *Cell* **165**, 813–826 (2016).

26. Lee, J. H., de Val, N., Lyumkis, D. & Ward, A. B. Model Building and Refinement of a Natively Glycosylated HIV-1 Env Protein by High-Resolution Cryoelectron Microscopy. *Structure* **23**, 1943–1951 (2015).

27. Chouaki Benmansour, N. *et al.* Phosphoinositides regulate the TCR/CD3 complex membrane dynamics and activation. *Sci. Rep.* **8**, 4966 (2018).

28. Costello, P. S., Gallagher, M. & Cantrell, D. A. Sustained and dynamic inositol lipid metabolism inside and outside the immunological synapse. *Nat. Immunol.* **3**, 1082–1089 (2002).

29. Xu, S. *et al.* Uptake of oxidized lipids by the scavenger receptor CD36 promotes lipid peroxidation and dysfunction in CD8+ T cells in tumors. *Immunity* **54**, 1561-1577.e7 (2021).

30. Kent, A., Longino, N. V., Christians, A. & Davila, E. Naturally Occurring Genetic Alterations in Proximal TCR Signaling and Implications for Cancer Immunotherapy. *Front. Immunol.* **12**, (2021).

Figures and Legends

Figure 1

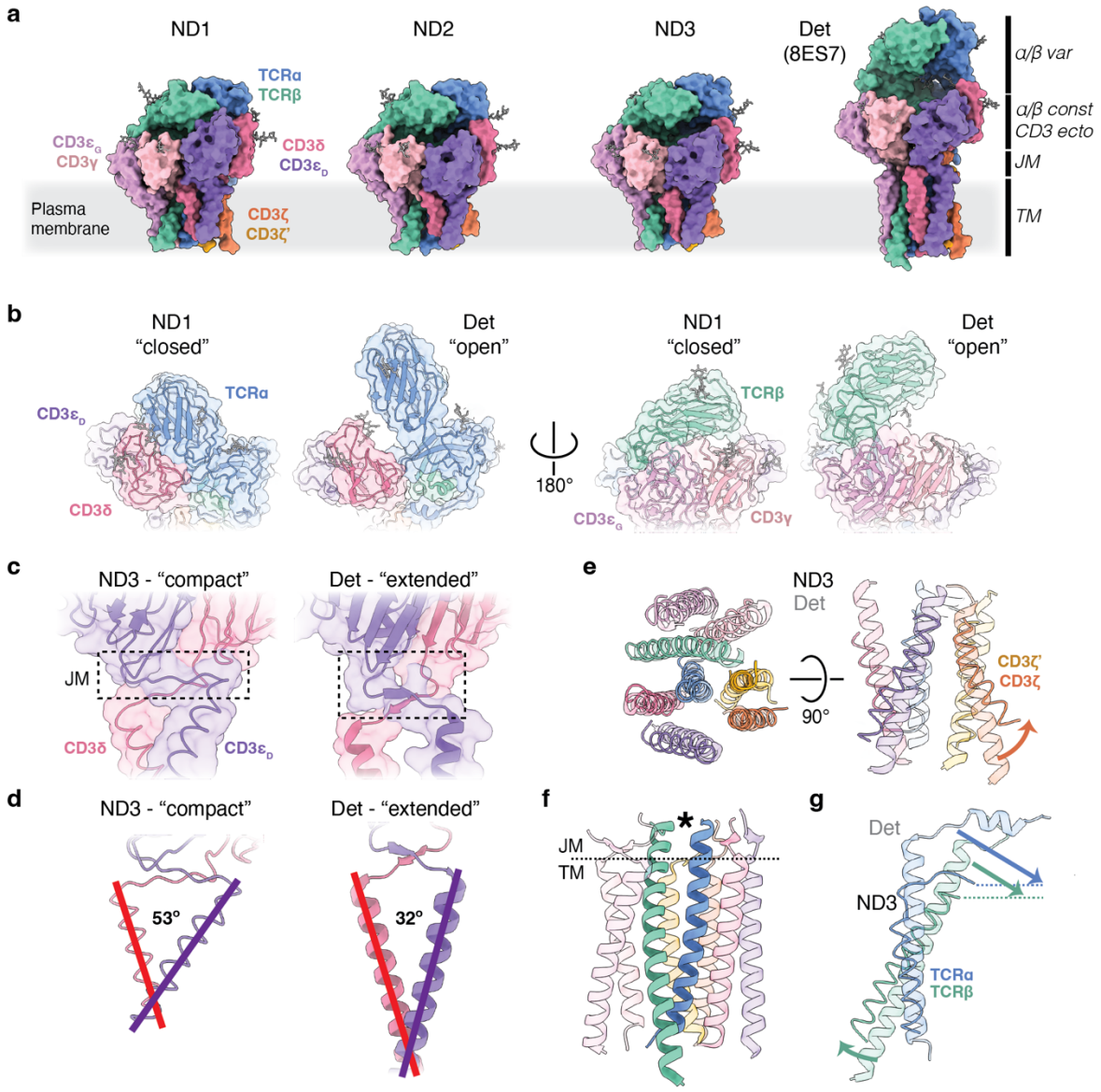

Figure 1: Architecture of the TCR in a native-like lipid environment. (a) Space-filling solvent-excluded surfaces for the models (herein, model surfaces) of the TCR in nanodiscs (conformations ND1, ND2, and ND3), compared with that in a detergent micelle (Det, PDB 8ES7). Protein regions indicated for the Det model: var, variable domains; const, constant domains; JM, juxtamembrane linkers; TM, transmembrane helices. Plasma membrane approximated by the 4-nm thick gray box, as aligned in Extended Data Figure 8b. (b) Comparison of ND1 and Det models, highlighting ectodomain closure in a lipid bilayer. Model backbone cartoon inside transparent model surfaces shown. (c) Comparison of ND3 and Det models, highlighting juxtamembrane linker compaction in the direction normal to the lipid bilayer (CD3εδ heterodimer pair shown). Backbone cartoon in transparent model surface shown. (d) Increased splay of the CD3εδ TM helices accompanying JM compaction. (e) Comparison of the TM helices in the detergent micelle (Det, transparent) and lipid bilayer (ND3, opaque), viewed from the extracellular space (left) and parallel to the membrane (right). Orange arrow highlights increased splay at the carboxy-terminal ends of the CD3ζ TM helices. (f) Cartoon representation of the TM and JM regions of the TCR in detergent (PDB 8ES7), highlighting the outward continuation of the TCRαβ TM helices (asterisk), where they are ensconced by the extended CD3 JM linkers. (g) Comparison of TCRαβ TM helices in Det (transparent) and ND3 (opaque), highlighting the unstructuring and downward deflection of the TCRαβ TM helix extensions (straight arrows). Curved arrow highlights TCRβ TM helix deflection.

Figure 2

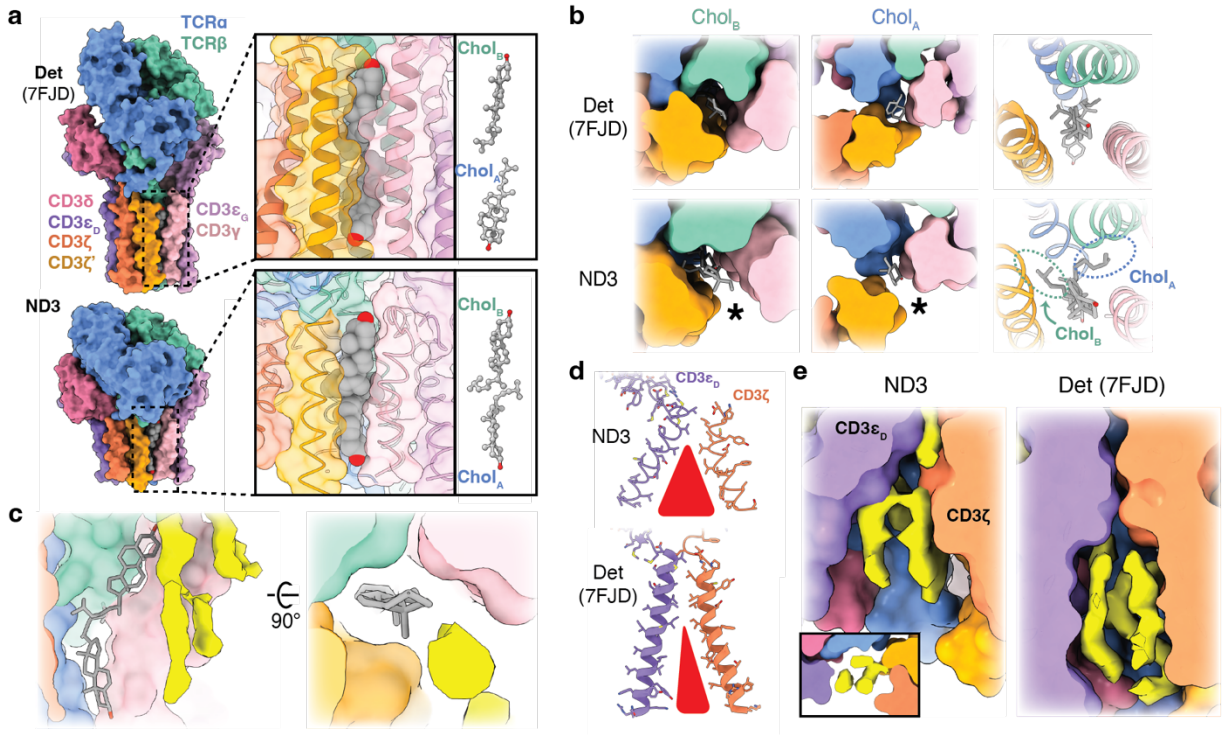
a
TCRα
TCRβ
Det
(7FJD)
CD3δ
CD3εD
CD3ζ
CD3ζ'
CD3εG
CD3γ
ND3
CholB
CholA
b
CholB
CholA
Det
(7FJD)
ND3
*
*
CholA
CholB
c
90°
d
CD3εD
CD3ζ
ND3
Det
(7FJD)
e
ND3
Det (7FJD)
CD3εD
CD3ζ

Figure 2: TCR–lipid interactions. (a) Comparison of the cholesterol-binding sites of the TCR in detergent (top) and in nanodiscs (bottom). Overview shown at left and insets show the cholesterol-binding sites in detail (left) and with protein removed (right) to highlight the deflection of the branched aliphatic tails. Cholesterol nomenclature as in Extended Data Figure 7. (b) Sections parallel to the membrane plane highlighting the opening of the cholesterol-binding groove to the lipid environment (left and middle) and intercalation of the deflected aliphatic chains between TM helices (right) in nanodiscs. (c) Unmodeled density (yellow) consistent with structured membrane lipids adjacent to the cholesterol-binding groove in nanodiscs. ND3 shown. (d) Splay of the CD3ζ and CD3ε_D TM helices in nanodiscs enlarges a cavity between them compared to that in the detergent structure (red schematic triangles). (e) This cavity is filled with membrane lipids (yellow densities) in the nanodisc structures and a similar arrangement of tubular densities in the detergent structure.

Figure 3

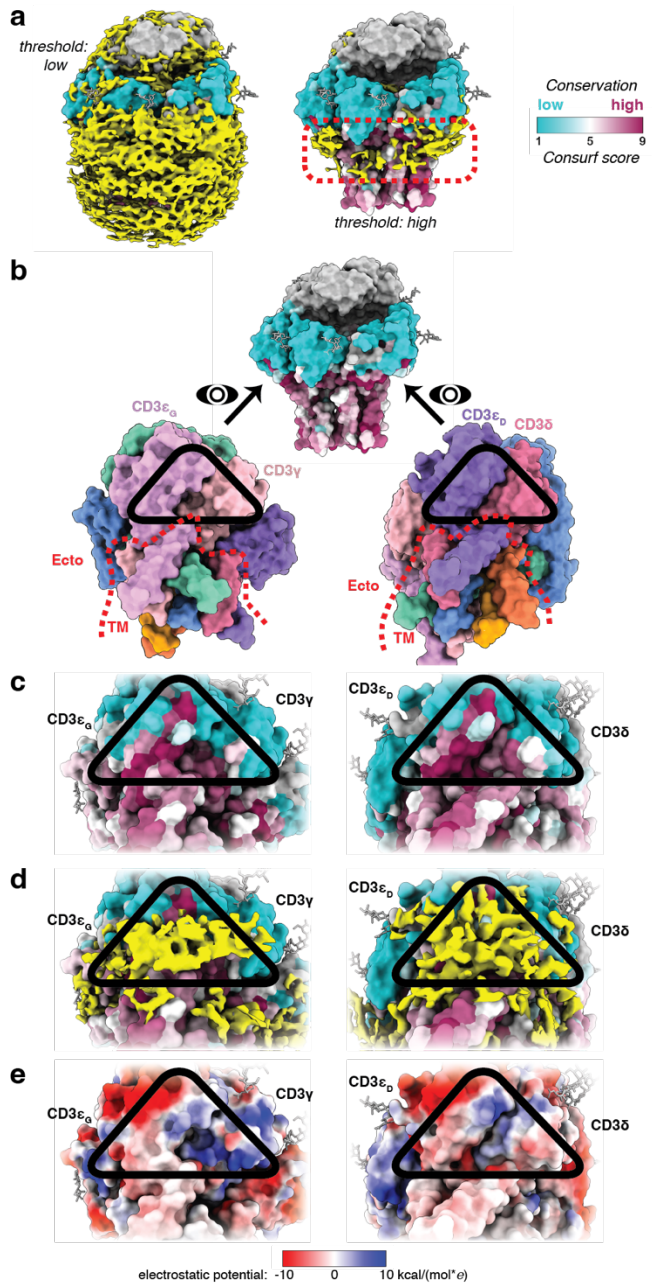
a
threshold: low
threshold: high
Conservation
low
high
1
5
9
Consurf score
b
CD3εα
CD3γ
Ecto
TM
CD3εD
CD3δ
Ecto
TM
c
CD3εα
CD3γ
CD3εD
CD3δ
d
CD3εα
CD3γ
CD3εD
CD3δ
e
CD3εα
CD3γ
CD3εD
CD3δ
electrostatic potential: -10
0
10 kcal/(mol*e)

Figure 3: Conserved CD3 surface patches form extensive membrane contacts. (a) ND3 model surface colored by sequence conservation (Consurf score 1 through 9) and yellow unmodeled map density from the nanodisc enshrouding the TCR TM helices and membrane-proximal ectodomain surfaces. When visualized with a higher contouring threshold (right), structured lipid density adjacent to the CD3 ectodomains persists (right, red dotted box). (b) Top, CD3 domains colored by conservation (same scale as panel a) reveal high relative sequence conservation in the CD3 TM helices and membrane-adjacent ectodomain surfaces, but not solvent-exposed surfaces. Arrows and eyes indicate the viewing direction for inspection of the CD3εγ and CD3εδ interfaces examined in the lower panels. Bottom, overviews orienting the close-up views in panels c through e. Red dashed lines denote the border between TM and ectodomain (Ecto) surfaces. (c) Close-up views of the membrane-proximal face of the CD3 heterodimers, with black triangles highlighting the conserved surface patch at the subunit interface. (d) Lipid density (yellow) that is most robust over this conserved patch. (e) The conserved ectodomain patch that is relatively electropositive compared to the surrounding ectodomain surfaces colored by electrostatic potential (red to blue, -10 to 10 kcal/(mol*e)).

Figure 4

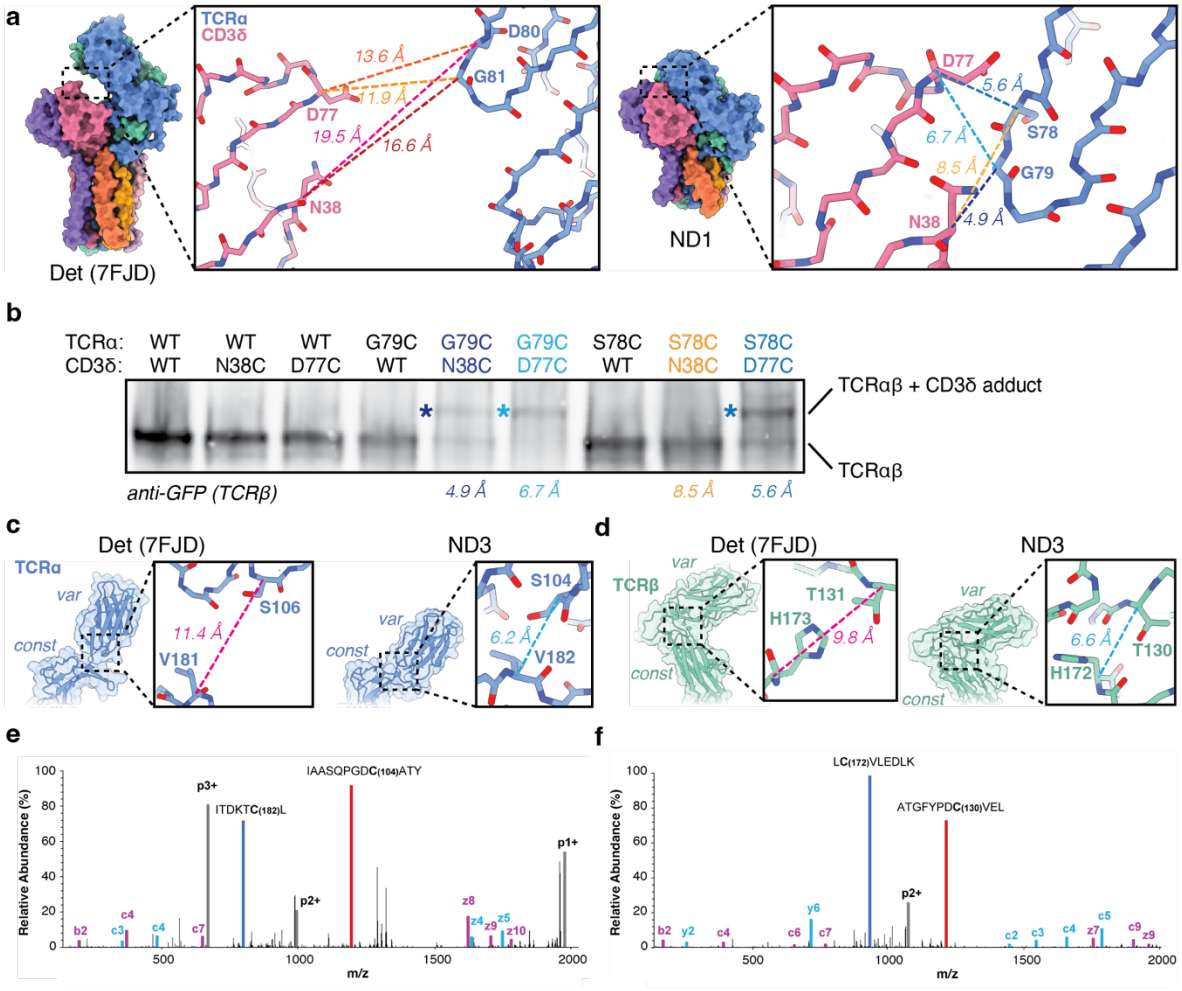
a
TCRα
CD3δ
13.6 Å
11.9 Å
19.5 Å
16.6 Å
D80
G81
D77
N38
Det (7FJD)
ND1
D77
5.6 Å
6.7 Å
S78
8.5 Å
G79
N38
4.9 Å
b
TCRα: WT WT WT G79C G79C G79C S78C S78C S78C
CD3δ: WT N38C D77C WT N38C D77C WT N38C D77C
TCRαβ + CD3δ adduct
TCRαβ
anti-GFP (TCRβ)
4.9 Å
6.7 Å
8.5 Å
5.6 Å
c
Det (7FJD)
ND3
TCRα
var
const
S106
11.4 Å
V181
S104
6.2 Å
V182
d
Det (7FJD)
ND3
TCRβ
var
const
T131
H173
9.8 Å
6.6 Å
T130
H172
e
IAASQPGDC(104)ATY
ITDKTC(182)L
p3+
p2+
p1+
Relative Abundance (%)
m/z
f
LC(172)VLEDLK
ATGFYPDC(130)VEL
p2+
Relative Abundance (%)
m/z

Figure 4: Confirmation of the TCR resting conformation *in situ.* (a) Comparison of Cα-Cα distances between apposing faces of CD3δ and TCRα in a lipid bilayer and in detergent highlighting plausible engineered disulfide positions in ND1 (distances in blue shades) that are not geometrically plausible in the open conformation (distances in yellow, orange, red, magenta). (b) Non-reducing SDS-PAGE of whole-cell lysates from HEK293T cells infected with the indicated TCR virus genotypes Western blotted for EGFP-tagged TCRβ. Engineered disulfides yielding a TCRαβ–CD3δ covalent adduct results in an upward gel shift (asterisks). Color coding and distances as in panel a. (c,d) Design of intrachain disulfides in the closed conformation of TCRα (c) and TCRβ (d). Distances color coded as above. (e,f) Mass spectrometric detection of intrachain disulfides in TCRα (e) and TCRβ (f). EThcD fragment spectrum of disulfide-linked dipeptide is shown. Gas-phase reduced linear peptides are shown in red (peptide A) and blue (peptide B) with the reduced Cys highlighted in bold. Fragment ions of the two linear peptides are shown in magenta (fragments of peptide A) and cyan (fragments of peptide B). Charge-reduced precursor ions are shown in gray.

Figure 5

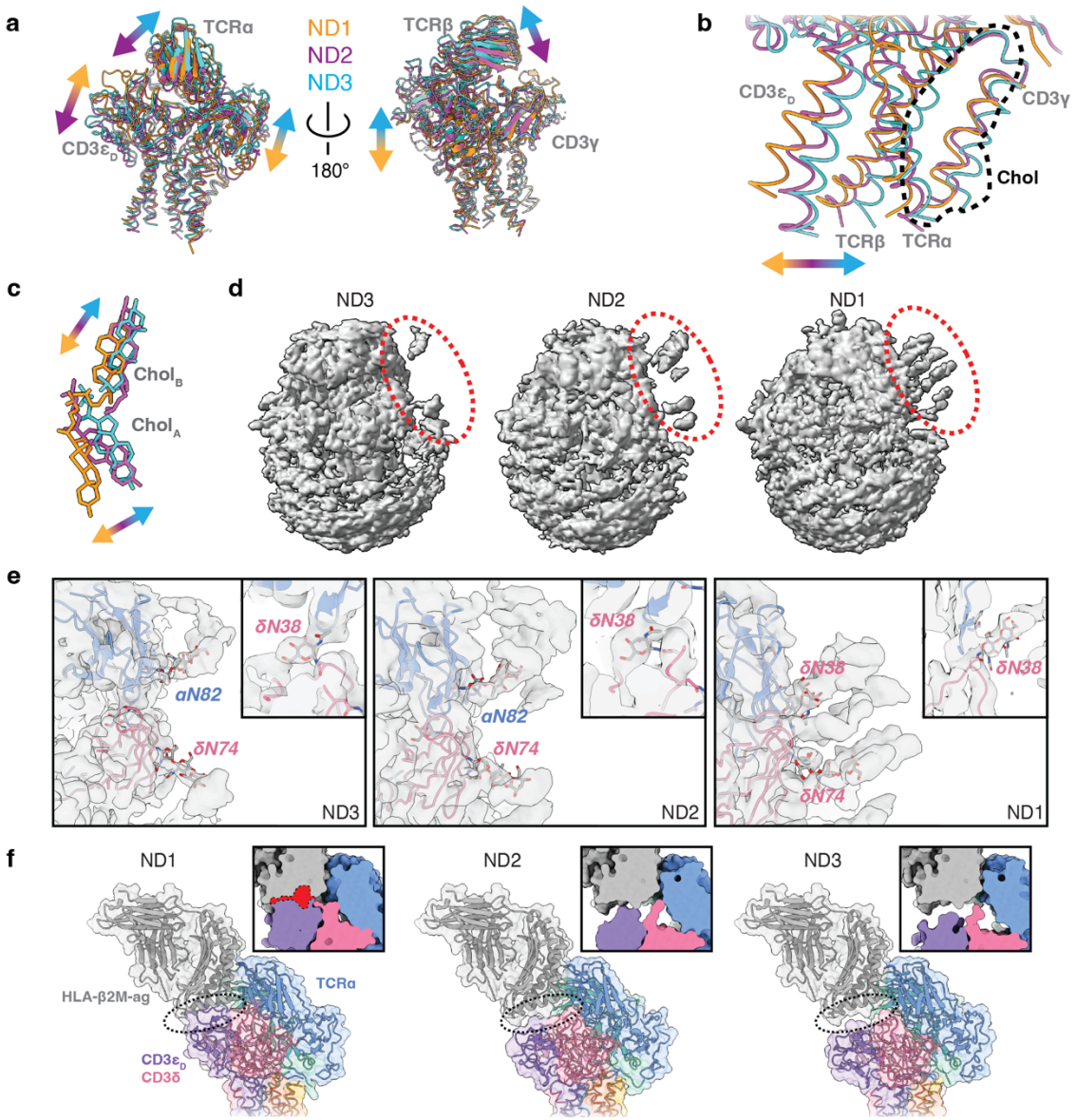
a
TCRα
ND1
ND2
ND3
TCRβ
CD3ε$_D$
180°
CD3γ
b
CD3ε$_D$
CD3γ
Chol
TCRβ
TCRα
c
Chol$_B$
Chol$_A$
d
ND3
ND2
ND1
e
δN38
αN82
δN74
ND3
δN38
αN82
δN74
ND2
δN38
δN38
δN74
ND1
f
ND1
HLA-β2M-ag
TCRα
CD3ε$_D$
CD3δ
ND2
ND3

Figure 5: Basal conformational variability of the TCR. (a) Comparison of models ND1-3, colored as indicated. Gradient arrows highlight the dominant ectodomain motions between each conformation in the ND1-ND2-ND3 series. (b,c) TM helix movement towards the cholesterol-binding site (dotted black line) in the ND series (b) and accompanying movements of the cholesterols (c). (d) Comparison of the TCRα–CD3δ lateral glycosylation sites (red dashed ovals) in the density maps showing increasing ordering of the glycan array with ectodomain closure. (e) Close-up view of the glycan array with cartoon model backbone and asparagine-linked glycan cores modeled. Insets highlight the position of the CD3δ N38 glycan, oriented inward in ND3 and ND2 but oriented outward in ND1. (f) Modeling HLA-β2M-antigen (ag, gray) binding to the TCR in conformations ND1-3. Dotted oval highlights area of clash between CD3ε_D and HLA in ND1, relieved by ectodomain opening in ND2 and 3. Insets show a cross-sectional view of model surfaces with the overlap of HLA and CD3ε_D shown in red.

Figure 6

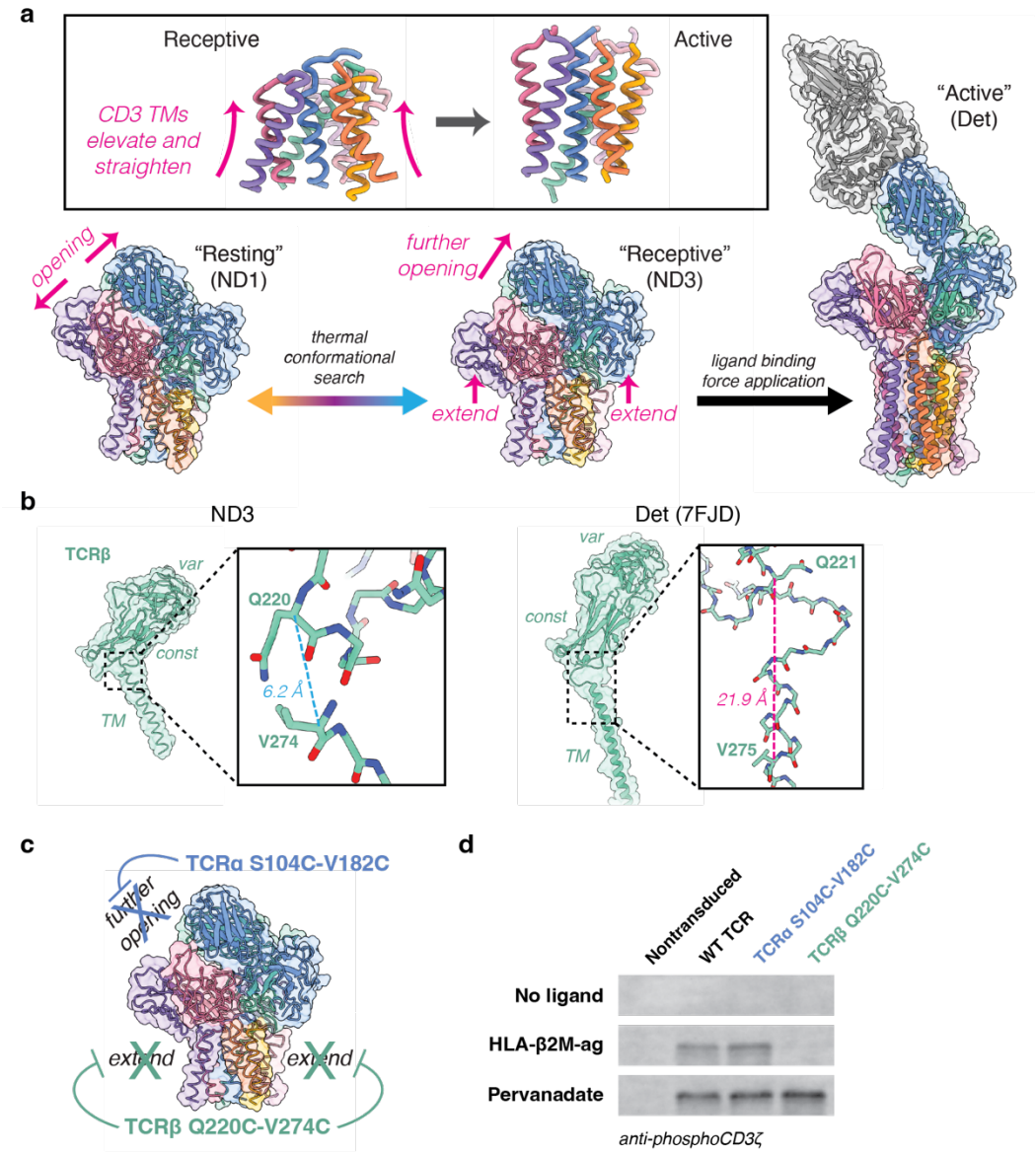
a
Receptive
Active
CD3 TMs elevate and straighten
"Active" (Det)
opening
"Resting" (ND1)
further opening
"Receptive" (ND3)
thermal conformational search
extend
extend
ligand binding force application
b
ND3
Det (7FJD)
TCRβ
var
const
TM
Q220
6.2 Å
V274
var
const
TM
Q221
21.9 Å
V275
c
TCRα S104C-V182C
further opening
extend
extend
TCRβ Q220C-V274C
d
Nontransduced
WT TCR
TCRα S104C-V182C
TCRβ Q220C-V274C
No ligand
HLA-β2M-ag
Pervanadate
anti-phosphoCD3ζ

Figure 6: Model of TCR activation. (a) Proposed model of TCR conformational dynamics. The unliganded TCR explores conformations with increasing receptiveness to ligand binding (ND1-ND2-ND3 series). Ligand-induced activation is mediated by a conformational transition from ND3 to an open, extended conformation. Inset highlights changes in the TM helix angles and positions between the ND3 to Det conformations, with TM helices becoming more parallel and the CD3 TM helices elevating relative to those of TCRαβ. Magenta arrows and text indicate movements required to transition to the next conformation in the series. (b) Design of an engineered disulfide in the compact conformation (cyan; left) not accessible in the extended conformation (magenta; right). (c) Schematic highlighting engineered disulfides to specifically impair either opening or extension between the proposed receptive and active conformations. (d) Western blot of whole-cell lysates from SUP-T1 cells transduced with the indicated TCRαβ-expressing virus reading out CD3ζ phosphorylation in response to the stimuli indicated at left.

Extended Data Figures and Legends

Extended Data Figure 1

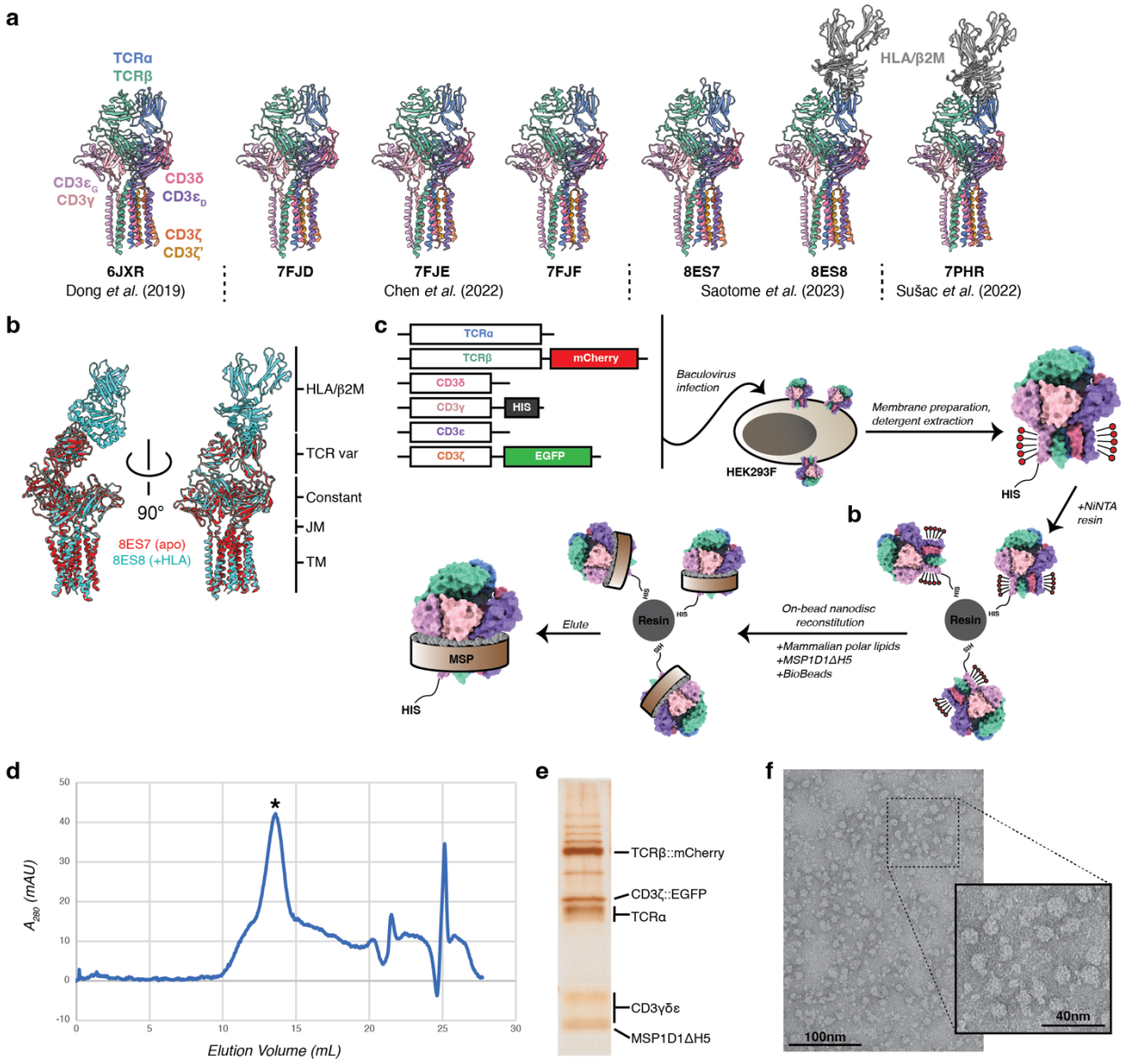

Extended Data Figure 1: Gallery of published TCR structures in detergent micelles, and expression, purification, and reconstitution of the TCR into lipid nanodiscs. (a) Cartoon representations of previously published structures of the TCR by itself and in complex with peptide-HLA-β2M determined in detergent micelles by cryo-EM. Models are colored by chain as indicated. (b) Superposition of published structures of TCR by itself (red) or in complex with peptide-HLA-β2M (cyan), showing no meaningful structural change throughout the TCR structure upon ligand binding. (c) Schematic representation of the expression and purification of TCR and its reconstitution into nanodiscs as described in Supplementary Methods. (d) Representative size-exclusion chromatogram of nanodisc-embedded TCR. Asterisk indicates peak of TCR in nanodiscs. (e) Representative silver-stained SDS-PAGE gel of pooled size-exclusion chromatography peak fractions. Constituents identified by expected molecular weight. CD3γ, δ, and ε cannot be distinguished by this approach. (f) Representative negative-stain electron micrograph of pooled size-exclusion chromatography peak fractions. Inset, zoomed-in view. Note presumed TCR density protruding from the circular nanodisc structures.

Extended Data Figure 2

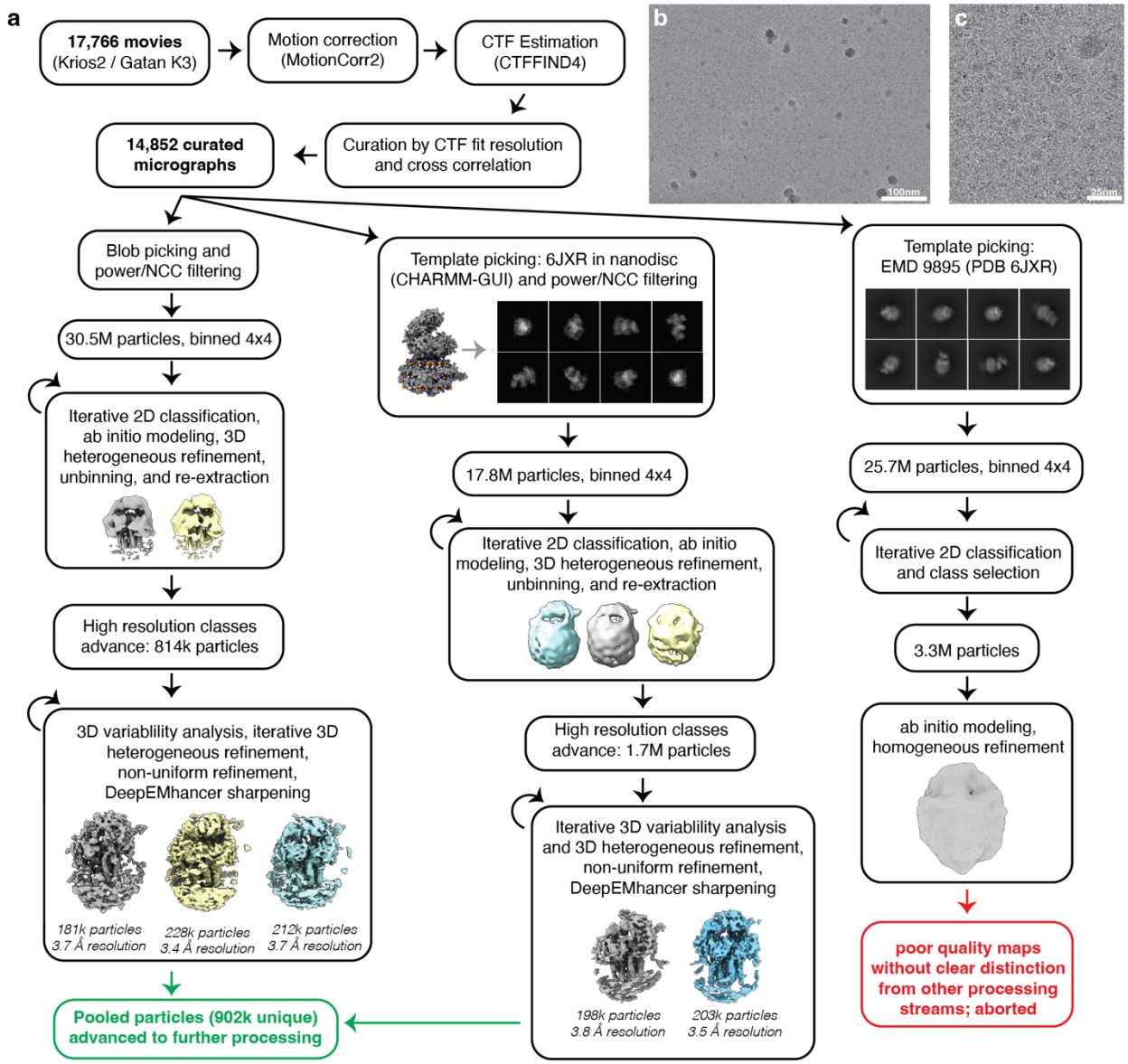

Extended Data Figure 2: Data collection and initial data processing. (a) Flow chart of data collection and image processing as described in Supplementary Methods. Data were processed in CryoSPARC v4 in three parallel streams using particle projections picked using an unbiased circular "blob" template (left), and using templates based on PDB 6JXR embedded in an MSP1D1ΔH5 nanodisc (center), or the original EM map used to create the PDB 6JXR model (right). The particle classes with the highest resolution reconstructions were pooled and advanced to further processing as detailed in Extended Data Figure 3. (b) Representative cryo-electron micrograph from this study. (c) Zoomed-in region of the image in (b).

Extended Data Figure 3

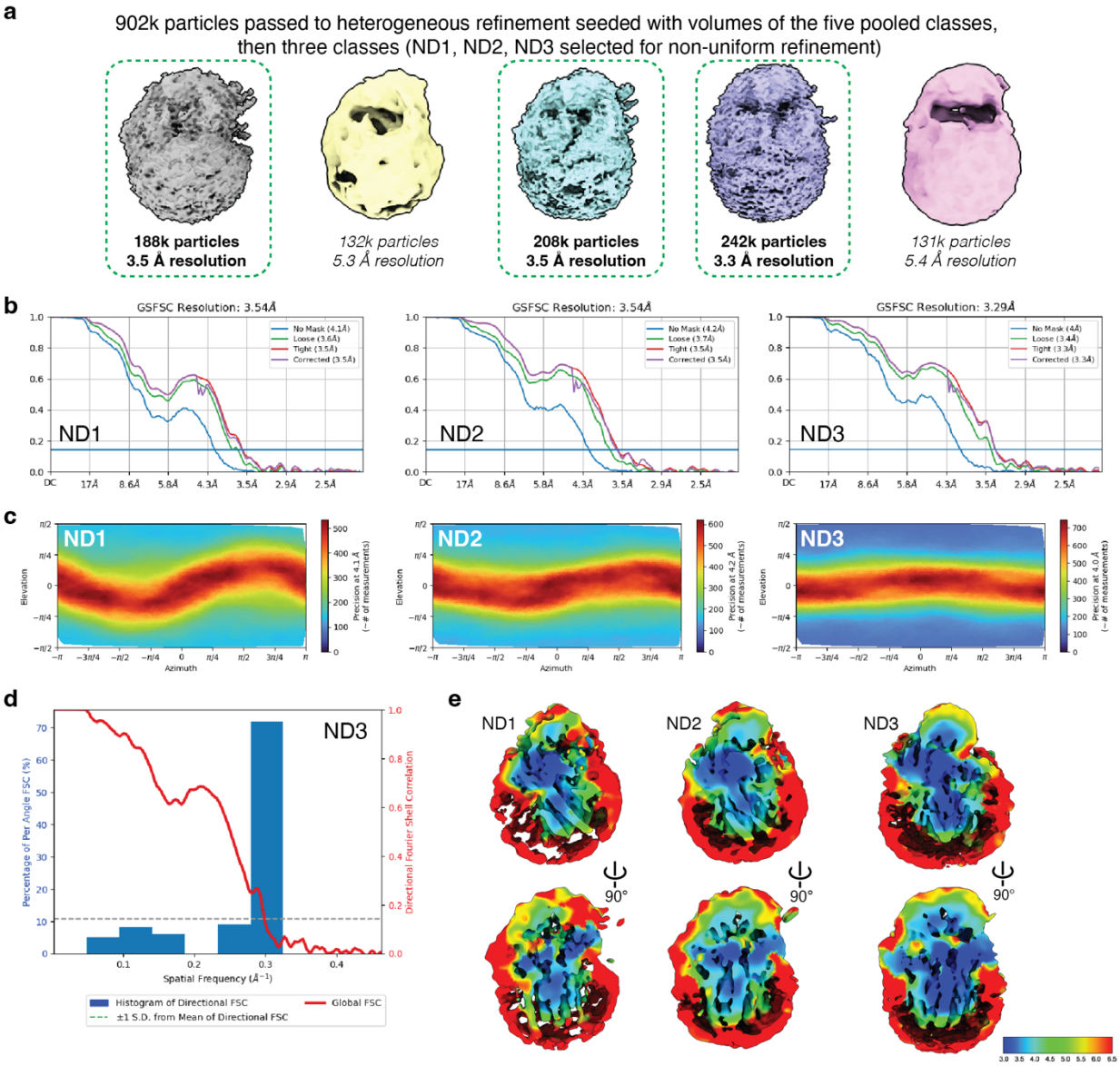

Extended Data Figure 3: Refinement of the density maps for the final three TCR classes. (a) Approximately 902,000 unique particles from the blob picking and TCR-in-nanodisc template picking processing streams (see Extended Data Figure 2) were pooled and their respective five maps were used to seed heterogeneous refinement in CryoSPARC. The five output maps were subjected to non-uniform refinement and the resulting maps are shown; ND1, ND2, and ND3 denote final refined classes. (b,c) Fourier shell correlations (b) and posterior precision directional distributions (c) for the final classes. While the posterior precision directional distributions show a degree of preferred particle orientation, the nominal resolution remained under 4 Å for most viewing directions (example in d). (d) 3D Fourier shell correlation direction histogram for ND3. (e) Local resolution estimates for the final maps, colored by resolution in Å.

Extended Data Figure 4

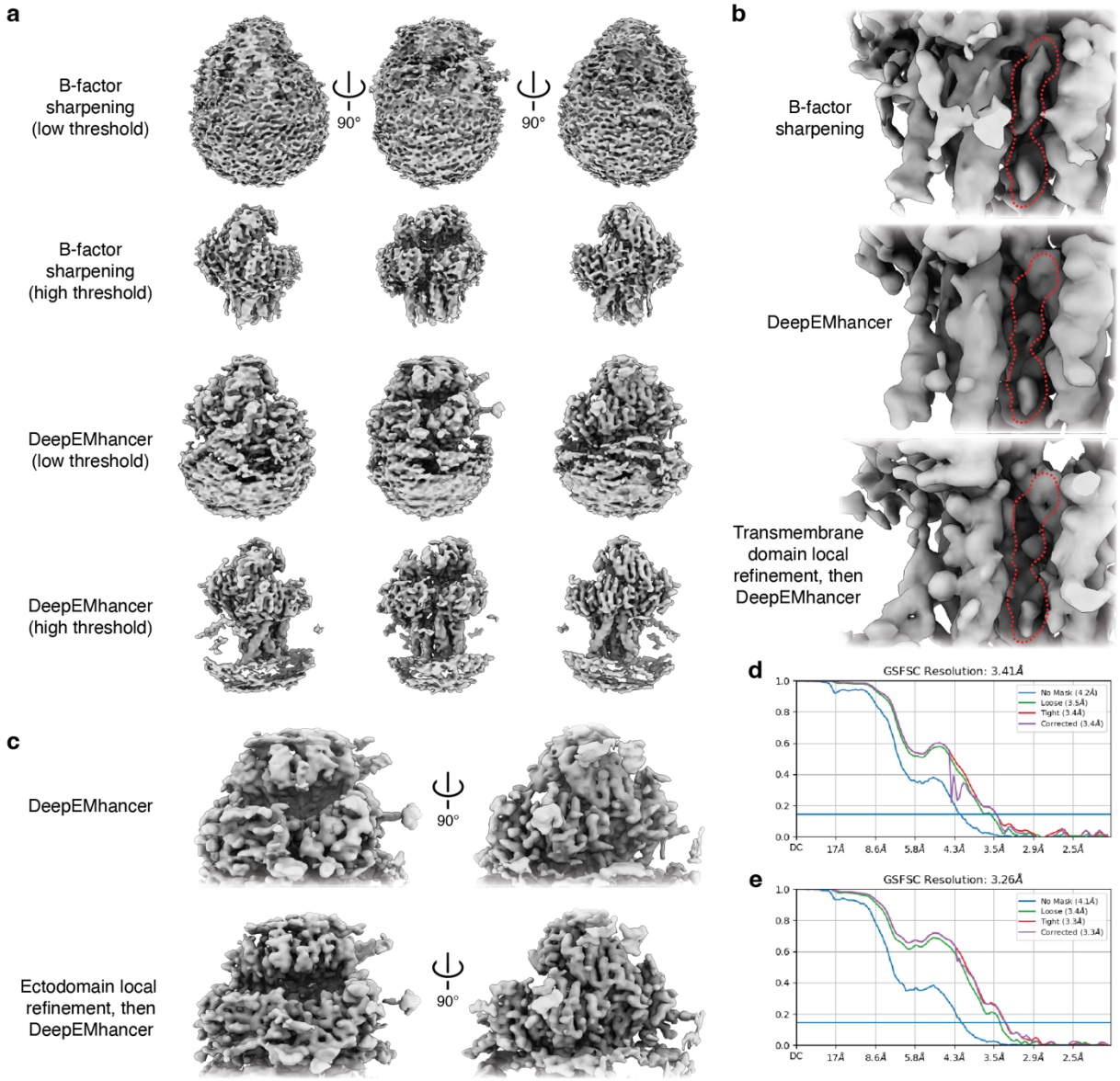

Extended Data Figure 4: Map post-processing. (a) Comparison of global B-factor sharpening and DeepEMhancer sharpening for ND3, with maps shown at high and low contouring thresholds. Note the better discrimination of the proteinaceous and glycan components by DeepEMhancer sharpening. (b) Lipid elements are better discriminated by global B-factor sharpening, with the volume for the cholesterol moieties in ND3 shown (red dotted boundaries). In contrast, note the further enhanced discrimination of the TM domains by local refinement and subsequent DeepEMhancer sharpening (bottom). (c) Similar improvement in the volumes corresponding to the CD3 and TCR ectodomains was observed with local refinement and DeepEMhancer sharpening. (d,e) Fourier shell correlation for local refinements of the ND3 TM helices (d) and ectodomains (e). Despite clear qualitative improvement in map interpretability, there was no improvement in nominal resolution.

Extended Data Figure 5

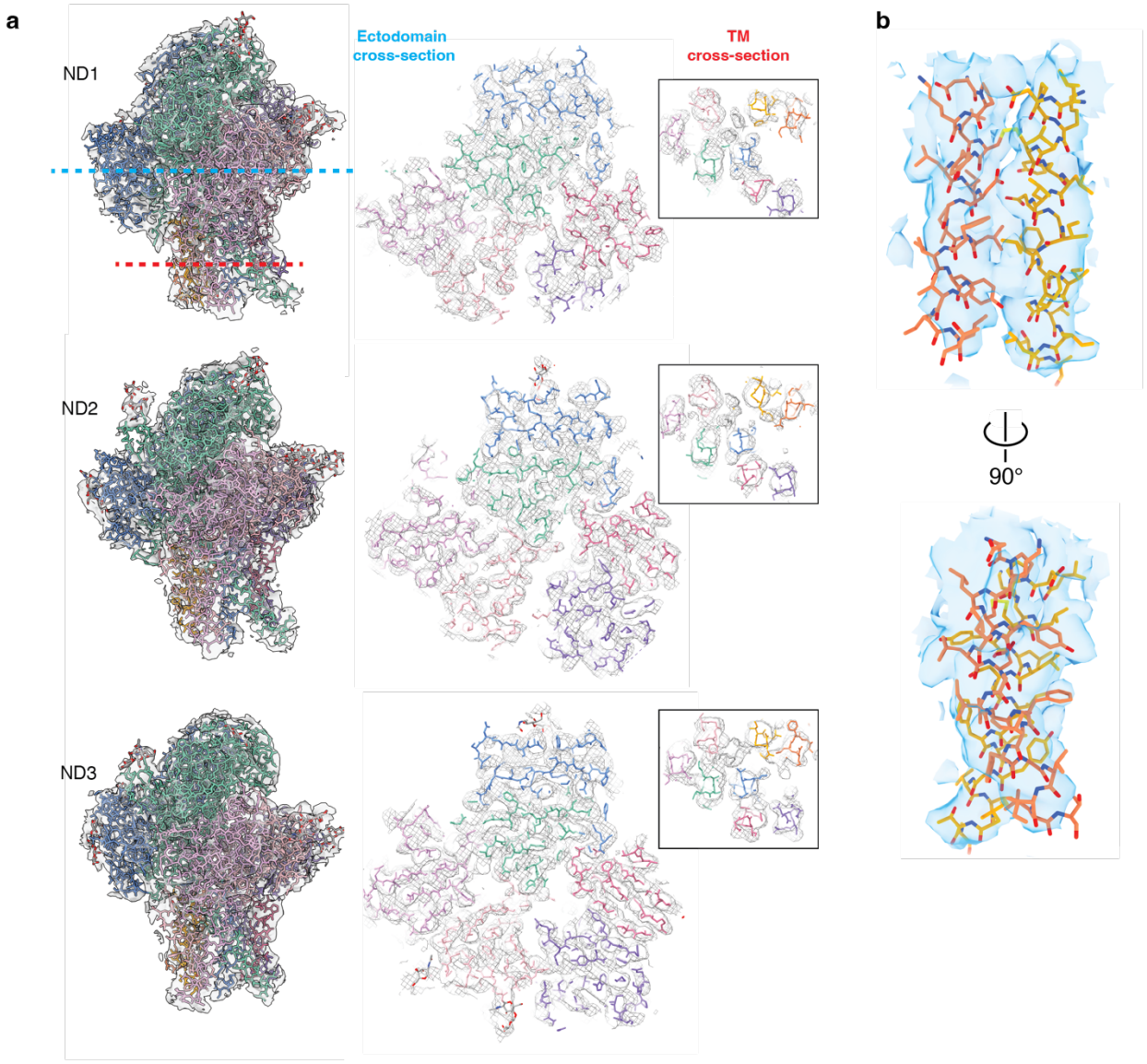

Extended Data Figure 5: Map-model fitting. (a) ND1, ND2, and ND3 models in their respective maps, clipped to a 3-Å zone around the model. Overview (left), and sections parallel to the membrane through the TCR ectodomains (center) and TM helices (right inset) at the approximate levels indicated in ND1. (b) DeepEMhancer-processed map with model for the TM helices of the CD3ζ dimer clipped to a 3.5-Å zone around the model.

Extended Data Figure 6

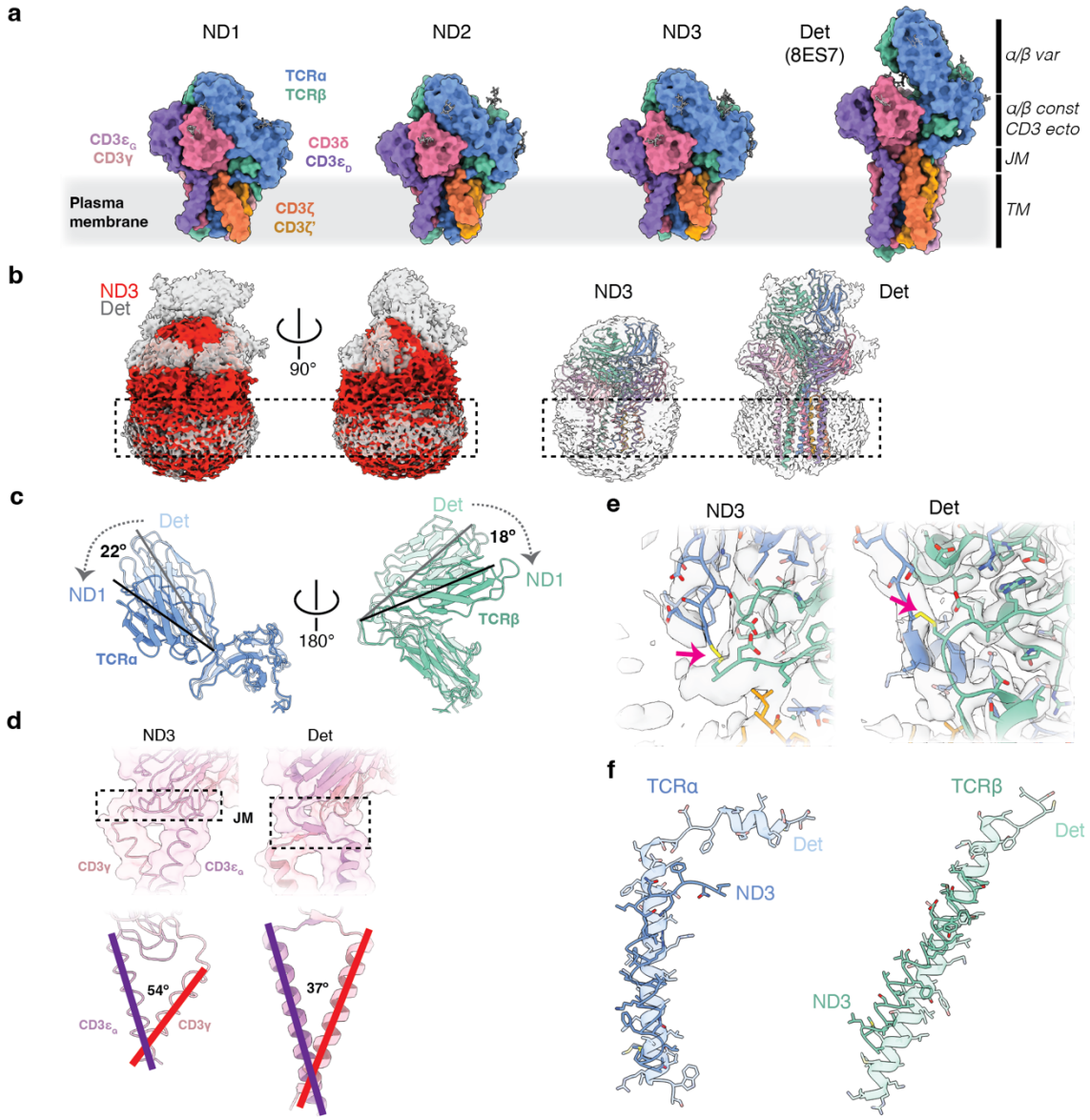

Extended Data Figure 6: Gross structural comparison of the TCR in nanodiscs and detergent. (a) Side views of model surfaces for ND1-3 in comparison to the TCR in detergent (PDB 8ES7). Plasma membrane approximated by the 4-nm thick gray box. (b) At left, overlay of the ND3 (red) and 8ES7 (Det, gray) maps manually aligned to the center of the micelle and nanodisc density to approximate plasma membrane insertion (dotted box). At right, cartoon models of the protein backbone are shown through transparent density maps. (c) TCRα (left, blue) and TCRβ (right, green) from ND1 (opaque) and 8ES7 (Det, transparent) aligned to their constant regions, highlighting a ~20º flexion at the interdomain hinge. (d) Comparison of the juxtamembrane (JM) linker region of CD3γ and CD3ε in ND3 and 8ES7 (Det), with accompanying comparison of their TM helices with interhelical angle shown (below). (e) Juxtamembrane linkers for TCRα and TCRβ, with backbone model shown in the density maps, for ND3 and 8ES7 (Det). For ND3, high-confidence modeling ends with the interchain disulfide (magenta arrow), whereas in 8ES7, the remainder of the JM linker is well structured. (f) TCRα (left, blue) and TCRβ (right, green) from ND3 (opaque) and 8ES7 (Det, transparent) aligned as in panel b, showing overall retained sequence register within the hydrophobic membrane/micelle milieu.

Extended Data Figure 7

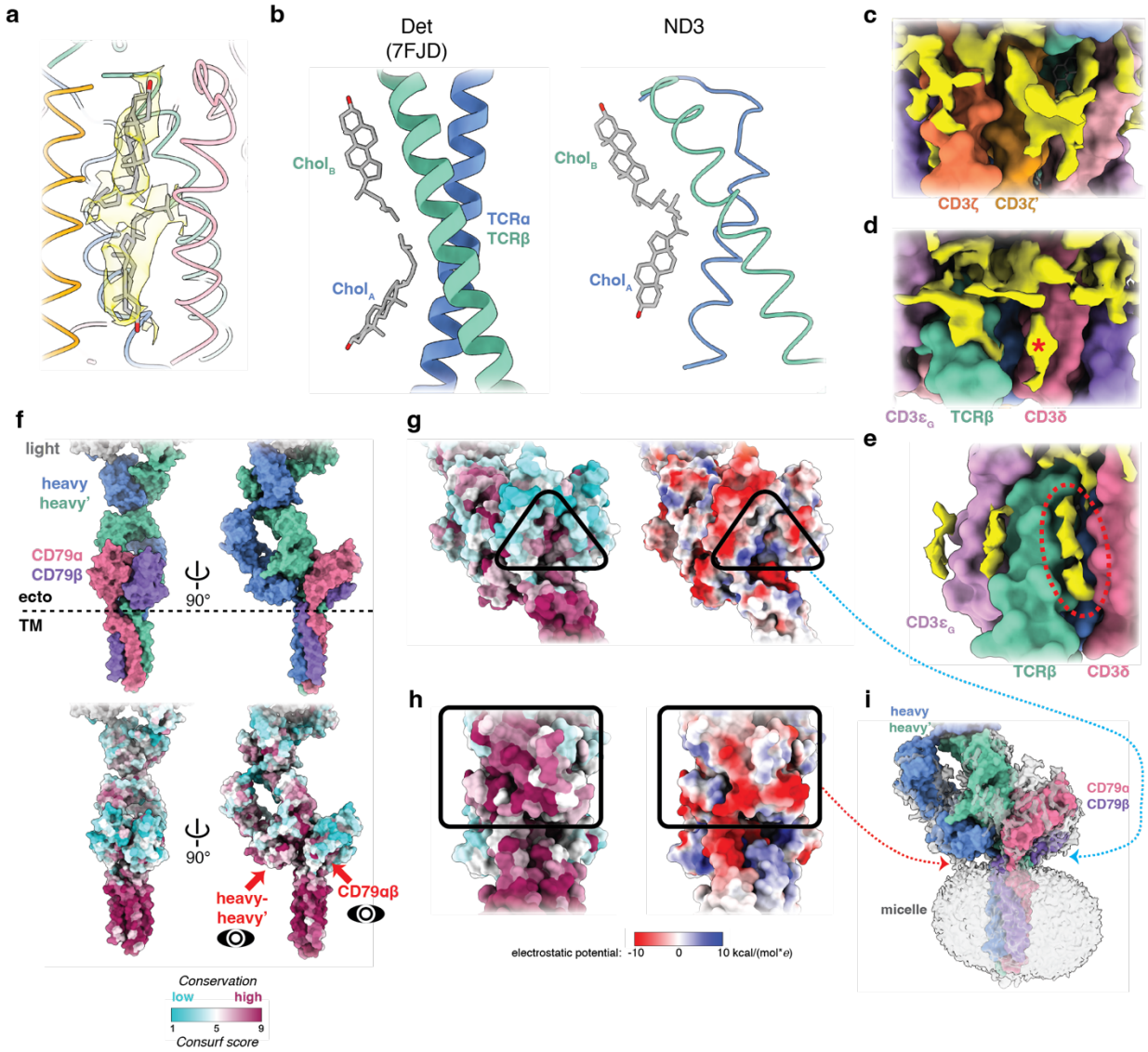

Extended Data Figure 7: TCR–lipid interactions and surface conservation analysis of the B-cell receptor. (a) Modeling of cholesterol into non-protein density (yellow). (b) Positioning of cholesterols adjacent to the TCR TM helices inspiring the nomenclature used here. (c,d) Additional possible structured lipid density in the outer leaflet surrounding CD3ζ,ζ' (c) and in the cleft between the CD3ε_G and CD3δ TM helices above the TCR TM helices that span this cleft (d). Red asterisk highlights density in the approximate position of the CD3δ Cys124 palmitoyl density seen in detergent (panel e). (e) PDB 7FJD surface representation with unmodeled density in yellow. Red dashed oval indicates density representing the Cys124 palmitoyl chain. (f) Surface representation of the human B-cell receptor (BCR) model, as determined in a detergent micelle by cryo-EM. Top, colored by chain; bottom, colored by sequence conservation (scale applies to remainder of figure). Red arrows and eye icons labeled CD79αβ and heavy-heavy' indicate the direction for the magnified views in panels (g) and (h), respectively. (g) Membrane-proximal face of the CD79αβ interface, colored by conservation (left, colored as in panel a) and electrostatic potential (right). Black triangle highlights region of high sequence conservation and corresponding surface electropositivity. However, this patch is oriented away from the micelle surface in the structure in detergent (dashed arrow to panel i). (h) Membrane-proximal face of the IgM heavy chains, with black box highlighting broad sequence conservation and largely electronegative conserved face. Dashed arrow indicates contact between this surface patch and the detergent micelle density in panel i. Electrostatic potential scale applies to panels g and h. (i) Surface model of the BCR with the unmodeled map density shown (transparent gray). Note the detergent micelle enshrouding the TM helices and making contact with the electronegative heavy-heavy' interface (red dashed arrow) but not the electropositive CD79αβ interface (blue dashed arrow), which is the opposite of what might be expected in a phospholipid membrane.

Extended Data Figure 8

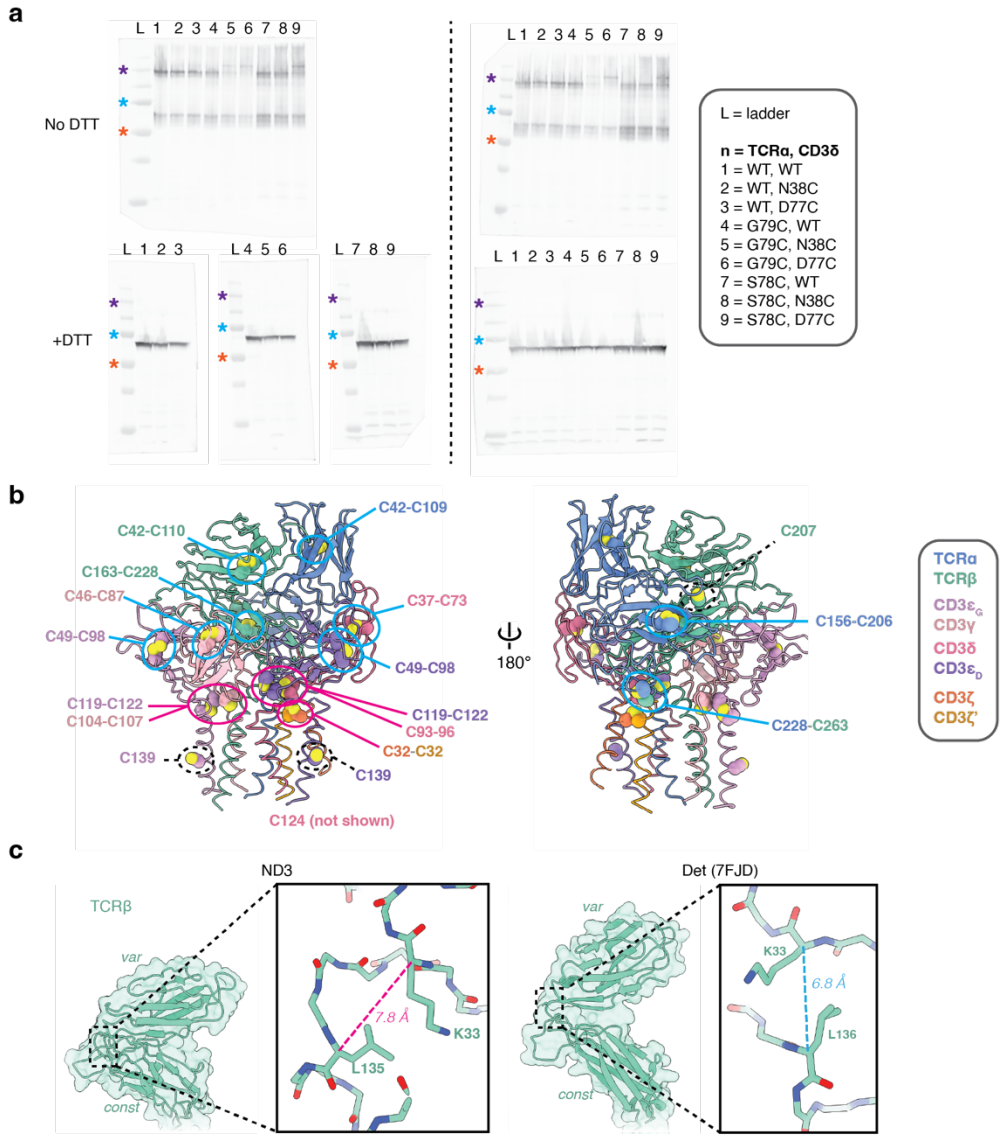

Extended Data Figure 8: Engineered disulfide crosslinking. (a) Full-length blots corresponding to the Western blot in Figure 4 (upper left) and a replicate (upper right). Additionally, blots were performed using lysates from the same infected cells boiled under reducing conditions ("with DTT"), showing disruption of the TCRαβ–CD3δ covalent complexes (bottom). Asterisks indicate the following molecular weight ladder values: purple, 150 kDa; cyan, 75 kDa; orange, 50 kDa. (b) Location of all native disulfides (solid cyan and magenta ovals) and unpaired cysteines (dashed black ovals) in this TCR construct. Disulfides indicated by cyan ovals are amenable to mass spectrometric detection as peptide pairs after EThcD, whereas disulfides indicated by magenta ovals are not unambiguously detectable by this approach, as they are C-X-X-C lariats or symmetric between CD3ζ homodimers. Subunits colored as indicated at right. (c) Design of an engineered disulfide bond plausible in the open Det conformation but not in the closed ND3 conformation.

Extended Data Figure 9

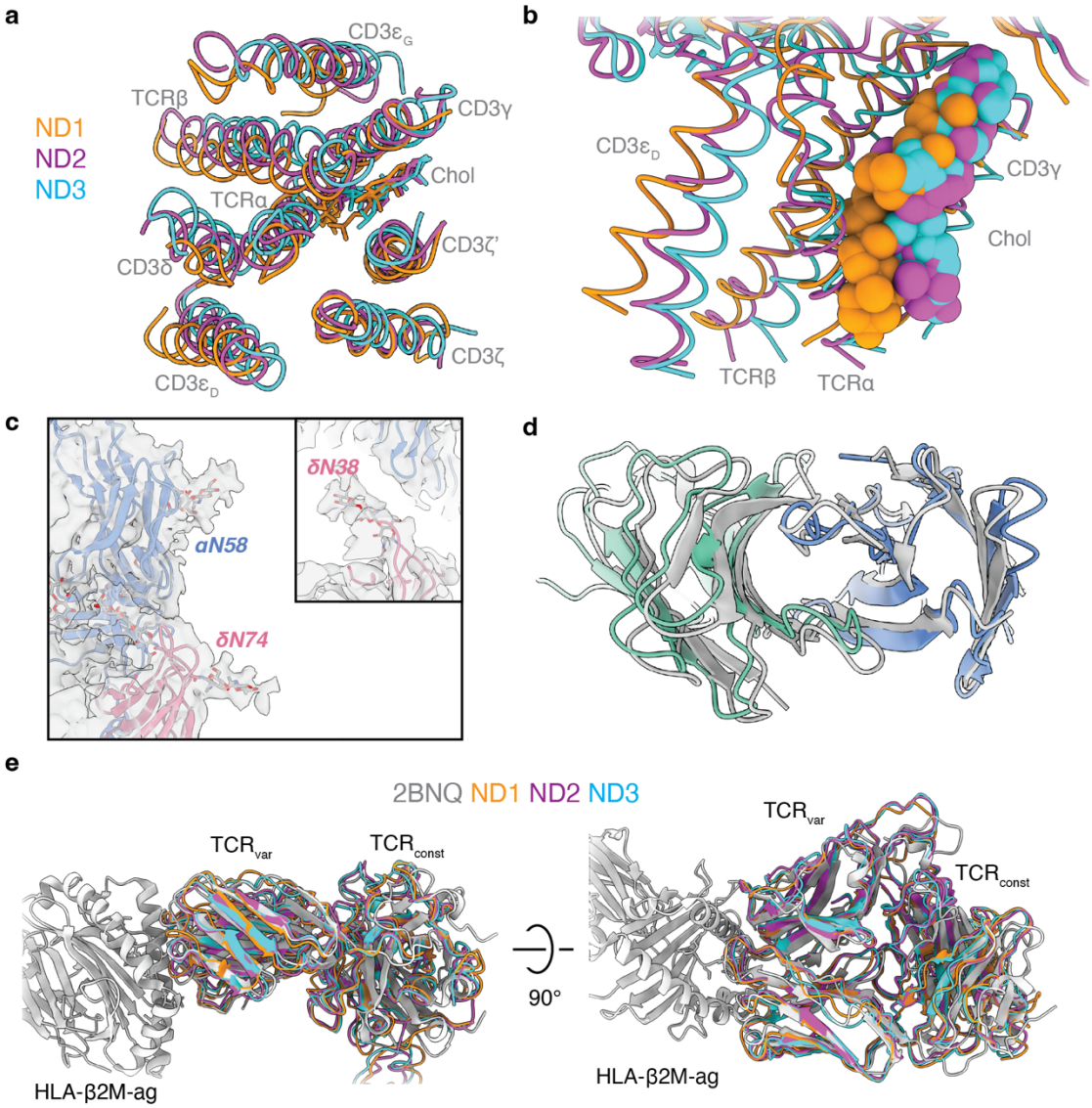

Extended Data Figure 9: Structural comparison of the ND1, ND2, ND3, and detergent conformations. (a) Model of the TCR TM helices and cholesterols in ND1-3, viewed from the extracellular face of the lipid bilayer. (b) Figure 5b reproduced with space-filling models of the cholesterols to delineate the cholesterol-binding pocket. (c) View of the lateral glycan array in the detergent conformation, with inset showing the inward position of the CD3δ N38 glycan. (d) Alignment of the TCR 1G4 crystal structure (gray) with the ND3 TCRα (blue) and TCRβ (green) variable domains, as viewed from the HLA-binding face. (e) Alignment of the ND1-ND3 models with the crystal structure of the HLA-bound TCR 1G4 crystal structure, showing a similar overall organization of the variable domains among the TCRs.

Extended Data Figure 10

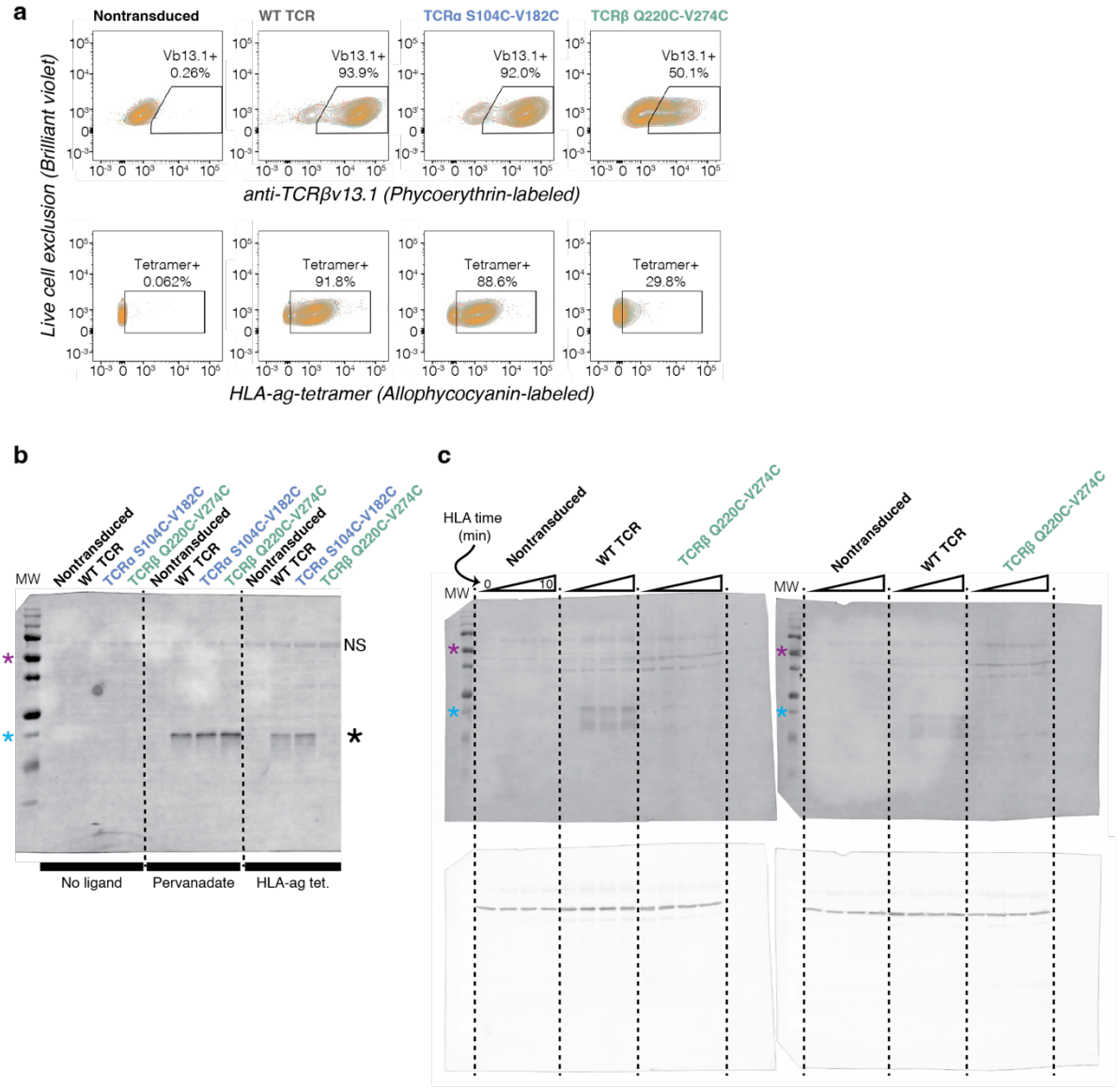

Extended Data Figure 10: Expression and HLA binding of mutant TCRs. (a) Representative flow cytometry plots of SUP-T1 cell lines transduced with the indicated TCR variants with labeling for surface TCRβ (top) and HLA-peptide tetramer binding (bottom row). (b) Full-length blot used to produce Figure 6d. Black asterisk indicates phospho-CD3ζ band. Nonspecific band (NS) serves as internal loading control. Colored asterisks indicate the following molecular weight ladder values: magenta, 50 kDa; cyan, 20 kDa. (c) Time course of SUP-T1 cell stimulation with HLA-antigen tetramers (0, 2, 5, 10 min left to right for each genotype) confirming absence of TCR activation by physiologic ligand in the locked-compact mutant. Replicate 1 on left and replicate 2 on right. Western blotting was performed against phospho-CD3ζ (top) and β-actin (bottom, loading control) on the same gels. Colored asterisks indicate the following molecular weight ladder values: magenta, 50 kDa; cyan, 20 kDa.

Extended Data Tables

Extended Data Table 1: Model building and refinement.

	ND1	ND2	ND3
Model			
Composition (#)			
Chains	10	12	12
Atoms	7788	7849	8014
Protein Residues	959	959	980
Water	0	0	0
Ligands			
BMA	4	7	7
NAG	13	15	16
CLR	2	2	2
Bonds (RMSD)			
Length (Å) (# > 4σ)	0.004 (0)	0.015 (5)	0.004 (0)
Angles (°) (# > 4σ)	0.927 (20)	1.47 (42)	0.968 (27)
MolProbity score	2.74	2.86	2.72
Clash score	35.51	44.62	35.07
Ramachandran plot (%)			
Outliers	0.75	1.07	1.15
Allowed	17.15	18.8	15.83
Favored	82.1	80.13	83.02
Rotamer outliers (%)	0.71	0.47	0.58
Cβ outliers (%)	0	0.22	0.11
Peptide plane (%)			
Cis proline/general	2.6 / 0.0	5.1 / 0.2	4.8 / 0.2
Twisted proline/general	0.0 / 0.0	0.0 / 0.1	0.0 / 0.4
CaBLAM outliers (%)	10.58	13.84	10.53
ADP (B-factors)			
Iso/Aniso (#)	7788 / 0	7849 / 0	8014 / 0
min/max/mean			
Protein	90.42 / 529.74 / 212.05	59.60 / 426.54 / 156.27	46.52 / 442.40 / 162.59
Ligand	168.95 / 669.71 / 341.81	61.38 / 487.72 / 202.38	64.11 / 402.16 / 227.78
Occupancy			
Mean	1	1	1
occupancy = 1 (%)	100	100	100
Data			
Box			
Lengths (Å)	93.96, 87.48, 103.68	91.80, 91.80, 103.68	95.04, 92.88, 105.84
Angles (°)	90, 90, 90	90, 90, 90	90, 90, 90
Supplied Resolution (Å)	3.5	3.5	3.2
Resolution Estimates (Å, Masked, Unmasked)			
d 99	4.7, 4.7	4.8, 4.9	4.5, 4.5
d model	3.4, 3.5	3.5, 3.5	3.3, 3.3.
d FSC model (0 / 0.143 / 0.5)	3.4 / 3.8 / 8.4, 3.4 / 3.8 / 8.9	3.5 / 3.9 / 8.6, 3.5 / 4.0 / 8.9	3.2 / 3.4 / 8.1, 3.2 / 3.8 / 8.3
Map values (min/max/mean)	-0.51 / 1.77 / 0.12	-0.62 / 1.69 / 0.12	-0.57 / 1.69 / 0.11
Model vs Data			
CC (mask)	0.58	0.55	0.57
CC (box)	0.67	0.67	0.68
CC (peaks)	0.4	0.44	0.47
CC (volume)	0.58	0.56	0.57
Mean CC for ligands	0.62	0.52	0.51

Extended Data Table 2: Disulfide-linked peptides identified by cross-linking mass spectrometry. Disulfide-linked peptides identified for each TCR genotype. Peptides with an XLinkX score greater than 30 are shown, as no native peptides were observed below this threshold. Color coding as follows: green, expected native disulfide; cyan, expected engineered disulfide; red, non-native disulfide or contaminant; magenta, non-native disulfide involving the engineered cysteines.

	XLINKX SCORE	SEQUENCE 1	CHAIN 1	CYS 1	SEQUENCE 2	CHAIN 2	CYS 2
TCRα(WT), TCRβ(WT)							
	120.57	V[C]LATGFYPDHVEL	B	163	[C]QVQFY	B	228
	106.91	LT[C]DAEAK	G	46	GMYQ[C]K	G	87
	95.96	Q[C]AQDMNHEY	B	42	F[C]ASSY	B	110
	90.84	T[C]PQYPGSEILW	E	49	VN[C]NTSITW	D	37
	73.16	FPSPESS[C]DVK	A	228	AD[C]GFTSESY	B	263
	70.28	SVPEGENLVLN[C]SFTDSAIY	A	42	L[C]AVRPLY	A	109
	69.67	SNKSDFA[C]ANAF	A	206	SV[C]LF	A	156
	58.32	T[C]PQYPGSEILW	E	49	[C]QVQFY	B	228
	53.59	VFVN[C]NTSITW	D	37	GIYR[C]NGTDIY	D	73
	40.68	NNSIIPEDTFFPSPESS[C]DVK	A	228	ATLV[C]L	B	163
	30.56	T[C]PQYPGSEILW	E	49	YV[C]YPR	E	98
TCRα(S104C-V182C), TCRβ(WT)							
	120.8	LT[C]DAEAK	G	46	GMYQ[C]K	G	87
	106.26	V[C]LATGFYPDHVEL	B	163	R[C]QVQFY	B	228
	104.38	Q[C]AQDMNHEY	B	42	F[C]ASSY	B	110
	92.7	GIYR[C]NGTDIYK	D	73	VFVN[C]NTSITW	D	37
	80.51	SVPEGENLVLN[C]SFTDSAIY	A	42	L[C]AVRPLY	A	109
	78.49	SNKSDFA[C]ANAF	A	206	SV[C]LF	A	156
	72.7	T[C]PQYPGSEILW	E	49	[C]QVQFY	B	228
	72.62	IAASQPGD[C]ATY	A	104	ITDKT[C]LDMR	A	182
	70.28	SVPEGENLVLN[C]SFTDSAIY	A	42	[C]NGTDIY	D	73
	65.27	V[C]LATGFYPDHVEL	B	163	T[C]PQYPGSEILW	E	49
	60.55	SDFA[C]ANAF	A	206	ITDKT[C]L	A	182
	56.37	FPSPESS[C]DVK	A	228	AD[C]GFTSESY	B	263
	49.26	ITDKT[C]L	A	182	SV[C]LF	A	156
	48.23	T[C]PQYPGSEILW	E	49	VN[C]NTSITW	D	37
	45.66	T[C]PQYPGSEILW	E	49	YV[C]YPR	E	98
TCRα(WT), TCRβ(T130C-H172C)							
	99.32	QEDGSVLLT[C]DAEAK	G	46	GMYQ[C]KGSQNK	G	87
	96.82	Q[C]AQDMNHEY	B	42	F[C]ASSY	B	110
	88.95	FGEGSRL[C]VLEDLK	B	130	ATGFYPD[C]VELSW	B	172
	79.2	SNKSDFA[C]ANAF	A	206	SV[C]LF	A	156
	72.18	SVPEGENLVLN[C]SFTDSAIY	A	42	L[C]AVRPLY	A	109
	71.14	GIYR[C]NGTDIYK	D	73	VFVN[C]NTSITW	D	37
	63.42	L[C]VLEDLK	B	130	LT[C]DAEAK	G	46
	62.17	L[C]VLEDLK	B	130	SV[C]LF	A	156
	54.2	L[C]VLEDLK	B	130	F[C]ASSY	B	110
	53.77	T[C]PQYPGSEILW	E	49	L[C]VLEDLK	B	130

	53.5	FPSPESS[C]DVK	A	228	AD[C]GFTSESY	B	263
	47.92	T[C]PQYPGSEILW	E	49	[C]QVQFY	B	228
	41.91	L[C]VLEDLK	B	130	[C]QVQFY	B	228
	41.51	AD[C]GFTSESY	B	263	L[C]VLEDLK	B	130
	38.79	T[C]PQYPGSEILW	E	49	YV[C]YPR	E	98
	36.32	ATGFYPD[C]VEL	B	172	[C]LSSR	B	207
	34.92	VFVN[C]NTSITW	D	37	GMYQ[C]K	G	87
	30.54	LT[C]DAEAK	G	46	[C]QVQFY	B	228
TCRα(WT), TCRβ(K33C-L135C)							
	96.43	GIYR[C]NGTDIYK	D	73	VFVN[C]NTSITW	D	37
	95.43	LT[C]DAEAK	G	46	GMYQ[C]K	G	87
	90.79	ATLV[C]LATGFYPDHVEL	B	163	R[C]QVQFY	B	228
	81.71	LTVLED[C]K	B	135	ATLV[C]L	B	163
	81.57	Q[C]AQDMNHEY	B	42	F[C]ASSY	B	110
	81.57	LTVLED[C]K	B	135	[C]QVQFY	B	228
	79.2	SNKSDFA[C]ANAF	A	206	SV[C]LF	A	156
	76.07	T[C]PQYPGSEILW	E	49	[C]QVQFY	B	228
	72.9	SVPEGENLVLN[C]SFTDSAIY	A	42	L[C]AVRPLY	A	109
	69.49	LTVLED[C]K	B	135	F[C]ASSY	B	110
	65.27	V[C]LATGFYPDHVEL	B	163	T[C]PQYPGSEILW	E	49
	64.22	ATLV[C]LATGFYPDHVEL	B	163	ATLV[C]LATGFYPDHVEL	B	163
	53.91	T[C]PQYPGSEILW	E	49	VN[C]NTSITW	D	37
	48.05	V[C]LATGFYPDHVEL	B	163	SDFA[C]ANAF	A	206
	47.05	LTVLED[C]K	B	135	SV[C]LF	A	156
	45.66	V[C]LATGFYPDHVEL	B	163	SV[C]LF	A	156
	43.9	T[C]PQYPGSEILW	E	49	V[C]YPR	E	98
	36.08	FPSPESS[C]DVK	A	228	AD[C]GFTSESY	B	263
	35.13	T[C]PQYPGSEILW	E	49	LTVLED[C]K	B	135
	35.04	T[C]PQYPGSEILW	E	49	[C]AVRPL	A	109
	34.06	V[C]LATGFYPDHVEL	B	163	VLN[C]SFTDSAIY	A	42
	30.82	SDFA[C]ANAF	A	206	LTVLED[C]K	B	135